ARTICLES
https://doi.org/10.1038/s41594-022-00786-8

nature structural & molecular biology

Check for updates

Structural insights into the lysophospholipid brain uptake mechanism and its inhibition by syncytin-2

Maria Martinez-Molledo[1,2], Emmanuel Nji[1] and Nicolas Reyes[1,2] ✉

Brain development and function require uptake of essential omega-3 fatty acids in the form of lysophosphatidylcholine via major-facilitator superfamily transporter MFSD2A, a potential pharmaceutical target to modulate blood–brain barrier (BBB) permeability. MFSD2A is also the receptor of endogenous retroviral envelope syncytin-2 (SYNC2) in human placenta, where it mediates cell–cell fusion and formation of the maternal–fetal interface. Here, we report a cryo-electron microscopy structure of the human MFSD2A–SYNC2 complex that reveals a large hydrophobic cavity in the transporter C-terminal domain to occlude long aliphatic chains. The transporter architecture suggests an alternating-access transport mechanism for lipid substrates in mammalian MFS transporters. SYNC2 establishes an extensive binding interface with MFSD2A, and a SYNC2-soluble fragment acts as a long-sought-after inhibitor of MFSD2A transport. Our work uncovers molecular mechanisms important to brain and placenta development and function, and SYNC2-mediated inhibition of MFSD2A transport suggests strategies to aid delivery of therapeutic macromolecules across the BBB.

The brain selectively exchanges solutes with the blood through a specialized BBB. BBB integrity is essential to cognitive function and prevents passage of neurotoxic molecules and pathogens, but it imposes major restrictions on delivery of therapeutic drugs into the brain[1,2]. Major-facilitator superfamily domain-containing 2A (MFSD2A) is selectively enriched at the BBB endothelium[3,4] and is the main uptake mechanism of docosahexaenoic acid (DHA)[3], an essential omega-3 fatty acid for brain and retina development and function[5–8]. MFSD2A transports esterified DHA in the form of lysophosphatidylcholine (LPC) in a Na^+-dependent manner[3,9]. The importance of MFSD2A transport function is highlighted by single-residue inactivating mutations in humans that cause severe microencephaly and intellectual disability[10–13]. Notably, Mfsd2a-knockout and Mfsd2a-mutant mice have a leaky BBB due to a selective increase in caveolar transcytosis, and reveal that Mfsd2a lipid transport is a key mechanism that controls BBB permeability and is important in normal BBB development and function[4,14–16]. Consistently, downregulation of MFSD2A is associated with the age-related increase in BBB permeability to neurotoxic proteins from plasma, and it could contribute to neurodegenerative diseases[17]. Thus, MFSD2A is a potential drug target for modulating BBB permeability and could aid in delivering therapeutic molecules into the brain[18], but selective transport inhibitors that could play this part have not been reported.

The MFSD2A transport cycle involves a series of conformational changes to bind and release LPC on opposite sides of the membrane, and recent cryo-electron microscopy (cryo-EM) structures of mouse (mm-Mfsd2a)[19] and chicken (gg-Mfsd2a)[20] orthologs offered a partial view of the cycle, revealing open outward- and inward-facing states, respectively. However, owing to a lack of structural information on important occluded intermediate states of the cycle, the MFSD2A lipid-transport mechanism remains incompletely understood, particularly regarding how LPC is translocated across the membrane. The mm-Mfsd2a structure suggested that only the LPC polar headgroup is translocated while bound to the transporter, with the lipid tail remaining in the membrane[19]. The gg-Mfsd2a structure proposed that the entire LPC molecule is occluded within the protein core[20].

In placenta, MFSD2A contributes to establishment and maintenance of a radically different cellular blood barrier, that at the maternal–fetal interface. In humans, this interface is formed by fusion of cells into a multinucleated-epithelial layer, namely syncytiotrophoblast (ST), directly bathed in maternal blood[21]. Strikingly, cell–cell fusion is achieved by a retroviral mechanism and is mediated by binding of envelope glycoproteins of retroviral origin, known as syncytin (SYNC), to cellular receptors[22–26].

SYNC2 is encoded by human endogenous retrovirus FDR (ERV-FDR), an extinct gamma-retrovirus that entered the simian lineage more than 40 million years ago, and is a homo-trimeric class-1 fusion protein that selectively uses MFSD2A as the cellular receptor[23,27]. Each SYNC2 protomer contains an amino-terminal surface subunit ($SYNC2_{SU}$) that binds MFSD2A, as well as a carboxy-terminal transmembrane subunit ($SYNC2_{TM}$) that conveys the membrane fusion machinery, including a transmembrane alpha-helix that anchors SYNC2 to the cell surface. The retroviral class-1 envelope fusion mechanism involves large conformational changes of the TM-subunit from so-called prefusion to post-fusion states[28,29]. In SYNC2, the post-fusion transition is somehow triggered by binding of $SYNC2_{SU}$ to MFSD2A, and the concomitant dissociation of the two subunits[30]. X-ray crystal structures of the $SYNC2_{TM}$ ectodomain revealed a 6-helix bundle arrangement typical of gamma-retroviral post-fusion state, consistent with the class-1 fusion mechanism[31,32]. However, $SYNC2_{SU}$ structure and its receptor-recognition mechanism remain unknown.

Here, we investigated human MFSD2A mechanisms using single-particle cryo-electron microscopy (cryo-EM) and functional approaches. The structure of the MFSD2A–SYNC2 complex and accompanying functional data reveal important molecular aspects of the MFSD2A transport cycle, the receptor-mediated cell–cell fusion mechanism, and pharmacology.

[1]Membrane Protein Mechanisms Group, European Institute of Chemistry and Biology, University of Bordeaux, CNRS-UMR5234, Bordeaux, France. [2]Membrane Protein Mechanisms Unit, Institut Pasteur, Paris, France. ✉e-mail: nicolas.reyes@u-bordeaux.fr

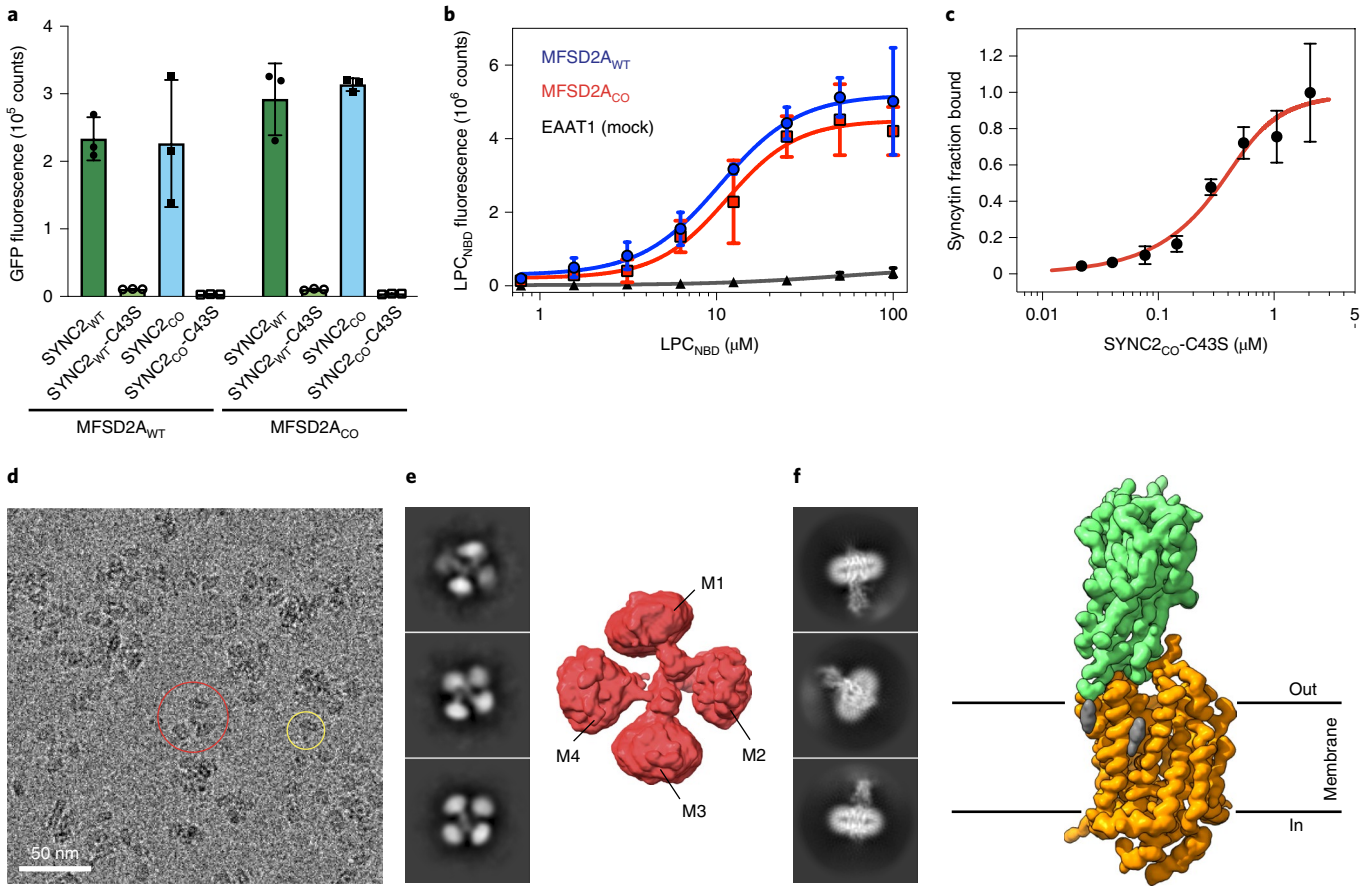

Fig. 1 | MFSD2A–SYNC2 functional and structural analyzes. a, GFP fluorescence arising from fusion of cells expressing $MFSD2A_{WT}$ or $MFSD2A_{CO}$ with those expressing SYNC2 constructs. **b**, Titrations of fluorescent-substrate analog (LPC_{NBD}) uptake in cells expressing $MFSD2A_{WT}$ (blue), $MFSD2A_{CO}$ (red), or negative-control excitatory amino acid transporter 1 (EAAT1; black). Solid lines are fits of the Hill equation. **c**, $SYNC2_{CO}$-C43S binding to $MFSD2A_{CO}$ in non-denaturing detergent solutions. The solid line is the fit of a binding quadratic equation. **d**, Example micrograph depicting extraction boxes (areas of interest extracted from the micrograph for analysis) corresponding to 3:3 $MFSD2A_{CO}$-$SYNC2_{CO}$-C43S (red circle) and 1:1 $MFSD2A_{CO}$-$SYNC2_{CO}$-SU complexes (yellow circle). **e**, Representative 2D classes and 3D reconstruction of 3:3 $MFSD2A_{CO}$-$SYNC2_{CO}$-C43S complex. **f**, Representative 2D classes and refined 3D cryo-EM map of 1:1 $MFSD2A_{CO}$-$SYNC2_{CO}$-SU complex. Densities corresponding to $MFSD2A_{CO}$ (orange) and $SYNC2_{CO}$-SU (green) are shown, as well as residual density (gray). Plots in **a**–**c** depict the average of three biologically independent experiments, and error bars represent s.e.m. Circles represent values from individual experiments (**a**) or average values (**b**,**c**).

Results

Cryo-EM structure determination. In order to obtain stable protein samples for in vitro complexation and structural analysis, we exchanged amino acids in the sequence of wild-type syncytin-2 ($SYNC2_{WT}$) and MFSD2A ($MFSD2A_{WT}$) for consensus residues of representative simian and vertebrate orthologs, respectively (Extended Data Fig. 1). Consensus designs, herein referred to as $MFSD2A_{CO}$ and $SYNC2_{CO}$, were more stable than their wild-type counterparts in non-denaturing detergent solutions (Extended Data Fig. 2a–d) and could be purified in milligram amounts with a high degree of homogeneity (Extended Data Fig. 2e). Importantly, $MFSD2A_{CO}$ and $SYNC2_{CO}$ show intact functional properties. First, we probed cell–cell fusion using a split-green fluorescent protein (GFP) complementation assay[33] in which green fluorescence reflects fusion of cells expressing different components of split GFP (Fig. 1a). Cell cultures co-expressing the GFP fragments with $SYNC2_{WT}$ ($SYNC2_{WT}$-$GFP_{1–10}$) and $MFSD2A_{WT}$ ($MFSD2A_{WT}$-GFP_{11}) yielded robust GFP-fluorescence signals, whereas a negative-control mutant ($SYNC2_{WT}$-C43S) that precludes $SYNC2_{SU}$ intra-subunit disulfide formation and cell fusion[30] showed negligible fluorescence levels. Indeed, cells co-expressing GFP fragments with consensus designs $SYNC2_{CO}$-$GFP_{1–10}$ and $MFSD2A_{CO}$-GFP_{11} (or any combination of consensus and wild-type constructs) revealed high-fluorescence signals, demonstrating that the fusogenic mechanism of $MFSD2A_{CO}$ and $SYNC2_{CO}$ is intact. We then probed $MFSD2A_{CO}$ transport function using an LPC fluorescent analog as a substrate (1-{12-[(7-nitro-2-1,3-benzoxadiazol-4-yl)amino] dodecanoyl}-2-hydroxy-sn-glycero-3-phosphocholine, referred to as LPC_{NBD})[3] (Fig. 1b). In the presence of sodium, $MFSD2A_{CO}$ showed robust LPC_{NBD} uptake levels, similar to $MFSD2A_{WT}$ and much larger than control cells expressing the unrelated Na^+-dependent neurotransmitter transporter EAAT1. Moreover, both $MFSD2A_{WT}$ and $MFSDA_{CO}$ GFP-fusion constructs localized to the plasma membrane and yielded similar cell-expression levels (Extended Data Fig. 2f,g). Importantly, $MFSD2A_{WT}$ and $MFSDA_{CO}$ showed nearly identical LPC_{NBD}-uptake concentration dependence, with half-maximal values of 11.9 ± 3.9 and 12.1 ± 2.4 μM, respectively (Fig. 1b). Overall, our functional experiments demonstrate that $MFSD2A_{CO}$ transport and receptor mechanisms are conserved.

For cryo-EM structural determination of the $MFSD2A_{CO}$–$SYNC2_{CO}$ complex, we used the $SYNC2_{CO}$-C43S mutant to avoid detachment of the surface and transmembrane subunits upon binding to the receptor. $SYNC2_{CO}$-C43S binds $MFSD2A_{CO}$ in non-denaturing detergent solutions with an apparent dissociation

Table 1 | Cryo-EM data collection and processing

	$MFSD2A_{CO}$–$SYNC2_{CO\text{-}SU}$ complex (EMD-12935) (PDB 7OIX)
Data collection and processing	
Magnification	105,000
Voltage (kV)	300
Electron exposure ($e^-/Å^2$)	47.1
Defocus range (μm)	−0.5 to −1.8
Pixel size (Å)	0.814
Symmetry imposed	none
Initial particle images (no.)	1,439,136
Final particle images (no.)	94,703
Map resolution (Å)	3.6
FSC threshold	0.143
Map resolution range (Å)	226–3.6
Refinement	
Initial model used (PDB code)	None
Model resolution (Å)	3.6
FSC threshold	0.143
Model resolution range (Å)	226–3.6
Map sharpening *B* factor ($Å^2$)	−40,62
Model composition	
Non-hydrogen atoms	5,869
Protein residues	716
Ligands	17
B factors ($Å^2$)	
Protein	158.36
Ligand	130.95
R.m.s. deviations	
Bond lengths (Å)	0.007
Bond angles (°)	1.015
Validation	
MolProbity score	1.70
Clashscore	8.81
Poor rotamers (%)	0.97
Ramachandran plot	
Favored (%)	96.48
Allowed (%)	3.52
Disallowed (%)	0.00

constant (K_D) of ~100 nM, yielding stable complexes for cryo-EM analysis (Fig. 1c and Extended Data Fig. 2e). Initial two-dimensional (2D) classes and three-dimensional (3D) reconstructions showed $MFSD2A_{CO}$–$SYNC2_{CO}$ complexes with four transmembrane components enclosed in separate detergent micelles, consistent with three $MFSD2A_{CO}$ molecules bound to trimeric $SYNC2_{CO}$ (Fig. 1d,e). However, high flexibility within the complex precluded high-resolution 3D reconstructions. To overcome this problem, we used a smaller box size in order to extract individual components, effectively increasing particle number and sample homogeneity, as was recently done in cryo-EM structure determination of human CD20 bound to divalent antibody fragments[34]. This approach enabled particle averaging over the three $MFSD2A_{CO}$ molecules in the complex, yielding a cryo-EM map at an overall ~3.6-Å resolution of the $SYNC2_{CO}$ surface subunit bound to $MFSD2A_{CO}$ (Fig. 1f, Table 1, and Extended Data Figs. 3 and 4). $SYNC2_{CO}$ transmembrane subunit ($SYNC2_{CO\text{-}TM}$) was not packed against the surface subunit ($SYNC2_{CO\text{-}SU}$), indicating that the former had undergone a transition to the post-fusion state, and that the two subunits remained linked through an inter-subunit disulfide bond as well as a long flexible linker. Trimeric $SYNC2_{CO\text{-}TM}$ in the post-fusion state was not resolved in the 3D cryo-EM reconstructions, likely owing to the lower number of particles as well as alignment problems of micelles containing only three flexible transmembrane helices.

Structure of MFSD2A in outward-facing occluded state. The structure of the $MFSD2A_{CO}$–$SYNC2_{CO\text{-}SU}$ complex was solved in the absence of the LPC substrate, and $MFSD2A_{CO}$ adopted an outward-facing occluded state in the transport cycle that displays a large central cavity between the transmembrane N and C domains. A cluster of highly conserved polar residues faces the bottom of this cavity near halfway across the membrane (Fig. 2a,b and Extended Data Fig. 5), and previous functional[3,9] and structural[19,20] studies have suggested that they are involved in binding the LPC polar headgroup (including Y56, Q57, R90, D93, Y151, E155, E312, S439, and K436) as well as in sodium coordination (D97 and T159).

The $MFSD2A_{CO}$ structure differs in several important aspects from that of the mm-Mfsd2a outward-facing open state[19] (Extended Data Fig. 6). The extracellular parts of the N and C domains in $MFSD2A_{CO}$ approach each other, closing the two lateral openings observed in mm-Mfsd2a between transmembrane-helix 2 (TM2) and TM11, as well as between TM5 and TM8, and occluding the central interdomain cavity from the membrane. Closer proximity between TM1 around F65 and the C domain, as well as contacts of the extracellular loop 3 (ECL3) with that domain, partially occlude the central cavity from the extracellular solution in $MFSD2A_{CO}$. During the open (mm-Mfsd2a) to occluded ($MFSD2A_{CO}$) transition, the N-terminal domain rotates nearly as a rigid body (<1 Å overall RMSD), but the C-terminal domain undergoes a notable conformational change in the extracellular part of TM7 that moves away from TM8–TM10, breaking several side chain contacts around conserved F315 (Supplementary Video 1). As a consequence of this, a shallow crevice observed on the mm-Mfsd2a C-domain surface expands into a large lateral cavity (~1,300 $Å^3$) within the C-terminal domain of $MFSD2A_{CO}$ (Extended Data Figs. 6 and 7). This cavity is mainly lined with conserved hydrophobic residues and directly connects to the polar-residue cluster through a constriction formed by F65, E312, L333, M337, and F399 (Fig. 2b,c and Extended Data Fig. 5).

The unique spatial arrangement of the polar-residue cluster, constriction, and lateral cavity appears optimal to bind and occlude LPC within the transporter from the outside. The D93/E155 and R90/K436 residue pairs are well positioned to provide counter-charges for the trimethyl-ammonium and phosphate groups of LPC head, respectively, while other residues in close proximity likely contribute to LPC-headgroup coordination (including Y56, Q57, Y151, E312, and S439). In turn, amino acid conservation and hydrophobicity in both constriction and the lateral cavity seem optimal to occlude the LPC fatty-acid tail into the C domain. In accordance, we were able to dock an LPC 18:3 molecule into $MFSD2A_{CO}$ structure with the phosphocholine moiety bound to the polar-cluster residue and with the glycerol group in close proximity to E312 and G313, while the lipid tail was partly wedged at the constriction (LPC C_{15}–C_{18}) and mainly occluded within the C-domain lateral cavity (LPC C_1–C_{14}) (Fig. 2b,c). Several lines of evidence further support binding of LPC to the above-mentioned structural elements: reported mutagenesis of residues in the central cluster, lateral cavity, and constriction have shown that they are important for transport[3,9,19,20]; transport-inactivating and disease-causing MFSD2A mutations in humans localize to the vicinity of central

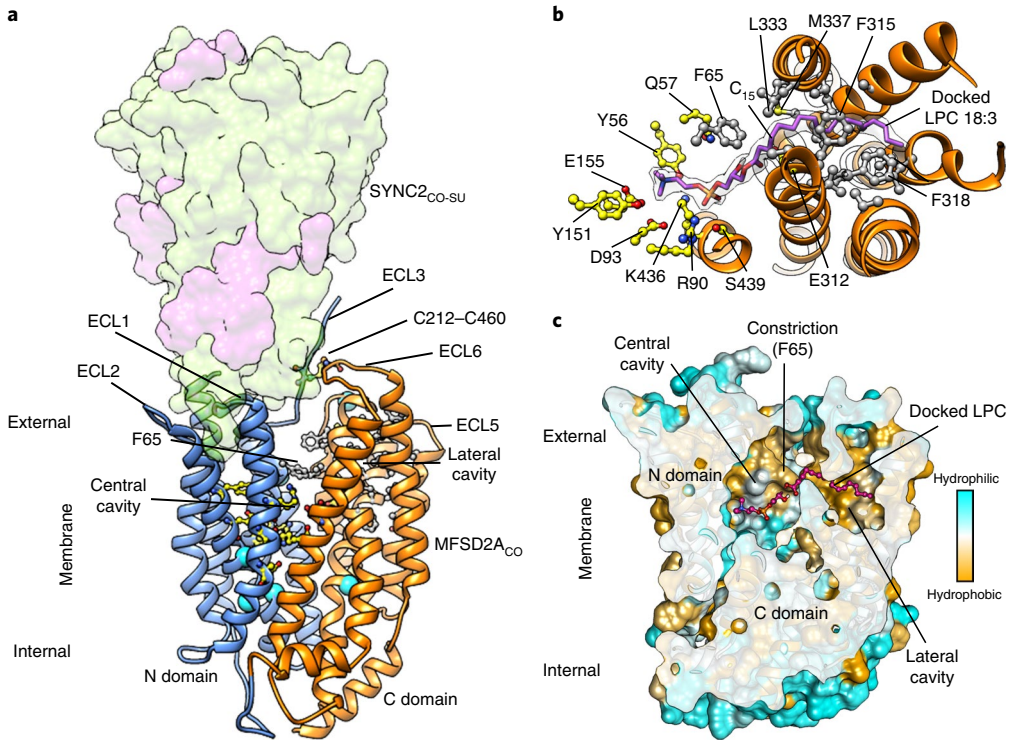

Fig. 2 | Outward-facing occluded MFSD2A. a, View of the membrane of the $MFSD2A_{CO}$–$SYNC2_{CO\text{-}SU}$ complex. N (blue) and C (orange) domains form an outward-facing cavity in $MFSD2A_{CO}$ displaying clusters of conserved polar (yellow) and hydrophobic (gray) residues. Human disease-causing MFSD2A mutations are mapped on the structure (alpha carbon, cyan spheres). **b**, Extracellular view of $MFSD2A_{CO}$ with docked LPC 18:3 molecule (purple, and pseudo-transparent molecular surface) burying lipid-tail C_1–C_{14} atoms within the C domain (orange ribbons). Residue side chains likely involved in binding of the LPC head group (yellow) and lipid tail (gray) are shown. N-domain TMs are not shown for clarity of display. **c**, MFSD2A molecular surface colored by residue hydrophobicity shows central and lateral cavities connected through a constriction around F65. $SYNC2_{CO\text{-}SU}$ is not shown.

(T159M, P164T, S166L) and lateral cavities (S339L, P402H, T198M, R326H)[10–13]; Na^+-dependent MFSD2 transporters that selectively carry sphingosine-1-phophate[35,36], namely MFSD2B, lack the acidic residue pair equivalent to D93/E155 in MFSD2A, and instead have glycine and glutamine residues (Extended Data Fig. 5), respectively, likely reflecting structural adaptations to accommodate a phosphate terminal group instead of the trimethyl-ammonium one in LPC; and the structure of prokaryotic MFS lipid transporter LtaA in the open outward-facing state has revealed a cluster of conserved polar residues to coordinate the substrate headgroup, and a large hydrophobic cavity in the C domain to accommodate the bulky lipid tail of the substrate[37] (Extended Data Fig. 7).

Structural comparison of $MFSD2A_{CO}$ and gg-Mfsd2a[20] shows that isomerization between outward- and inward-facing states occurs through rotations of N and C domains around the central polar-residue cluster, alternately exposing central and lateral cavities to the extracellular and intracellular sides (Extended Data Fig. 6), and resembling a classical MFS 'rocker-switch' mechanism[38,39]. Interestingly, upon isomerization to the inward-facing state, movements around the extracellular part of TM7 relative to other TMs in the C domain decrease the volume of the lateral cavity and expand the constriction (Extended Data Fig. 7 and Supplementary Video 2), suggesting that these changes contribute to release the substrate on the cytoplasmic side. In accordance, the gg-Mfsd2a cryo-EM map shows non-protein density for a bound LPC molecule, with part of the acyl chain (C_1–C_5) bound to the constriction and the 'shrunk' lateral cavity volume, while the headgroup faces the cytoplasm and is loosely wedged in a cytoplasmic crevice between TM5 and TM8.

The above structural comparison shows that MFSD2A adapted a classical MFS rocker-switch mechanism[38,39] to translocate both the LPC headgroup and acyl chain occluded within the transporter (discussed below), resembling the recently proposed transport mechanism of bacterial MFS lipid transporter LtaA[37]. Differences in C-domain cavity size and dynamics between bacterial and mammalian MFS transporters likely reflect evolutionary adaptations of a conserved mechanism to transport different lipid substrates.

Structure of endogenous retroviral $SYNC2_{CO\text{-}SU}$. The structure of $SYNC2_{CO\text{-}SU}$ represents a distinct protein fold, and a search of the Protein Data Bank[40] showed only marginal resemblance to surface glycoproteins (GPs) from unrelated filoviruses (for example ebola virus, EBOV). Moreover, the AlphaFold protein structure database[41] produced a low-confidence $SYNC2_{SU}$ model that failed to predict the experimentally determined fold, likely owing to high amino acid conservation among $SYNC2_{SU}$ simian-homolog sequences and a low number of these sequences, as well as a lack of available structures that resemble the $SYNC2_{SU}$ fold.

$SYNC2_{CO\text{-}SU}$ is arranged in two domains: a core and a receptor-binding domain (RBD) (Fig. 3a,b and Extended Data Fig. 8). The core is a distorted beta barrel that encloses a small central alpha-helix (α_C), and it is capped on the opposite side of the RBD by N-terminal α_N. Several loops pack around the distorted beta barrel and establish disulfide bonds with β2 (C126–C145), β11 (C291–C308), and β14 (C301–C317). Extensions from core structural elements form the RBD. This domain is a concave five-stranded anti-parallel β-sheet that partly enwraps α_R. Notably, the three loops connecting β1–α_R, β4–β5, and β10–β11 constitute the main contact region with MFSD2A, and we refer to them as receptor-binding loops 1–3 (RBL1–RBL3).

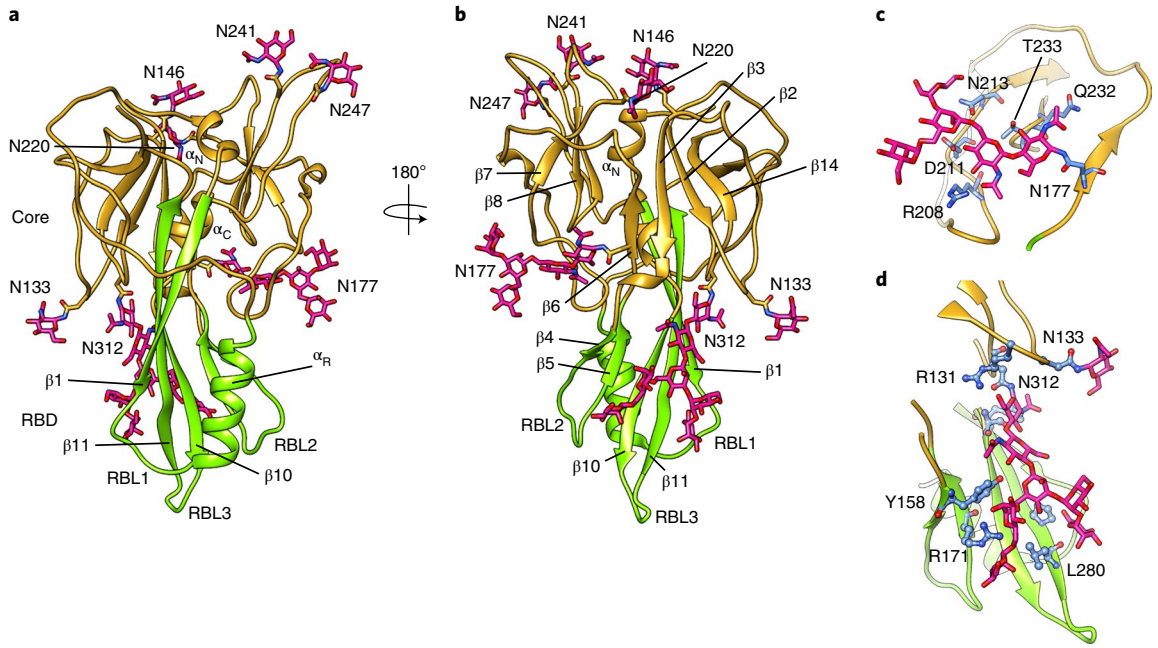

Fig. 3 | SYNC2$_{CO\text{-}SU}$ structure and glycan coat. a, SYNC2$_{CO\text{-}SU}$ structure displaying core (gold) and RBD (green). All seven predicted N-glycosylation sites display glycans (pink). **b**, Approximately 180° rotation along the SYNC2$_{CO\text{-}SU}$ long axis from **a**, showing the side where glycans concentrate on SYNC2$_{CO\text{-}SU}$ surface. **c**, Glycan N177 interacts with residues (blue) in the core. **d**, Glycan N312 interacts extensively with the RBD in close proximity to the MFSD2A$_{CO}$ binding interface (not displayed).

SYNC2$_{CO\text{-}SU}$ displays extensive N-glycosylation on its surface, resembling to some extent the 'glycan coat' observed in envelopes of exogenous and infectious human retroviruses[42]: glycans at N146, N220, N241, and N247 in the core are distant from the MFSD2A interface and are solvent-exposed. In stark contrast, the glycans at N177 and N312 are cradled in cavities on the SYNC2$_{SU}$ surface and remain more structured, displaying cryo-EM density that enabled modeling of high-mannose glycan molecules. N177 glycan binds a pocket delimited by loops between β6–β7 and β8–β9 in the core, and contributes to stabilize its fold through several contacts (Fig. 3c). In turn, N312 binds a shallow pocket in the RBD and adopts a striking position in close proximity to RBL2 and RBL3 (Fig. 3d). Notably, SYNC2$_{SU}$ glycans concentrate on one side of its surface (Fig. 3b), suggesting that the side devoid of these molecules provides the interface to interact with SYNC2$_{TM}$ in the prefusion state (Fig. 3a).

SYNC2–MFSD2A binding interface. SYNC2$_{CO\text{-}SU}$ binds MFSD2A$_{CO}$ through an extensive network of interactions that buries a large and hydrophilic surface area of the MFSD2A$_{CO}$ N domain (~1,200 Å^2). The long axis of SYNC2$_{CO\text{-}SU}$ is nearly parallel to that of the transporter and is normal to the membrane plane, and the three RBLs of SYNC2$_{CO}$ interact with poorly conserved residues in crevices on MFSD2A$_{CO}$ surface (Fig. 4a, Extended Data Fig. 9, and Supplementary Table 1).

RBL1 and α$_R$ in SYNC2 lean towards the central cavity of the transporter, and RBL1 occupies a crevice between ECL1 and ECL3, partly occluding MFSD2A$_{CO}$ interdomain cavity through RBL1 residues K83–M86 (Fig. 4b). M86 is the only residue that contacts both ECL3 and ECL1, while K83 occupies the entrance of MFSD2A$_{CO}$ central cavity and constitutes a contact point of SYNC2$_{CO}$ with the C domain of MFSD2A$_{CO}$. RBL1 residue W78 forms an aromatic stack with F213 in ECL3, and the position of RBL1 is further stabilized through interactions between residues W78 and N90 and ECL3, as well as those between residues L85 and M86 and ECL1. RBL2 is the shortest loop in the RBD, and residues N164 and Q165 at its N-terminal end make contacts with the extracellular part of TM6. At the C-terminal end of RBL2, the R167 sidechain inserts into a crevice between ECL1 and ECL2, stabilized by contacts with residues in those loops, as well as electrostatic interactions (Fig. 4c). Notably, the longer RBL3 interacts more extensively with the ECL1–ECL2 crevice through residues V272–F276 (Fig. 4d). The side chain of SYNC2$_{CO}$ F275, and to a lesser extent that of F276, adopts a striking position tightly wedged in a pocket between TM2 and TM4 and fully inserted into the hydrophobic core of the micelle, in contact with a non-protein density likely corresponding to detergent or lipid molecules. The position of RBL3 within the membrane plane suggests a direct role for membrane lipids in SYNC2 receptor binding. Consistent with the structural observation that all RBLs extensively engage in MFSD2A$_{CO}$ recognition, poly-alanine mutants in RBL1–RBL3 targeting residues buried at the SYNC2$_{CO\text{-}SU}$–MFSD2A interface decreased SYNC2$_{CO}$ fusogenic function (Fig. 4e).

Another important feature of the SYNC2$_{CO\text{-}SU}$ binding interface is the close proximity of glycan N312 to RBL2 and RBL3. The position of this glycan, with its arms wrapping around β10–β11 and establishing contacts with β4–β5, strongly suggests that glycan N312 stabilizes interactions between those loops and MFSD2A$_{CO}$. In agreement with this, the glycosylation knock-out mutant SYNC2-N312Q, as well as SYNC2-N133Q that positions just atop, impaired cell–cell fusion activity[43].

Overall structural and functional results converge to show that SYNC2 establishes a complex network of protein-protein contacts with MFSD2A, mainly on the surface of the N-terminal domain, that are further stabilized by protein-lipid and protein-glycan interactions.

Binding of SYNC2$_{SU}$ inhibits MFSD2A transport function. The binding mode of SYNC2$_{CO\text{-}SU}$ appears to preclude important conformational changes of the MFSD2A transport cycle. ECL3 in MFSD2A, as well as RBL1 and α$_R$ in SYNC2$_{SU}$, partly occupy the space between the N and C domains of the transporter on the extracellular side, and steric clashes would prevent rotation of the domains

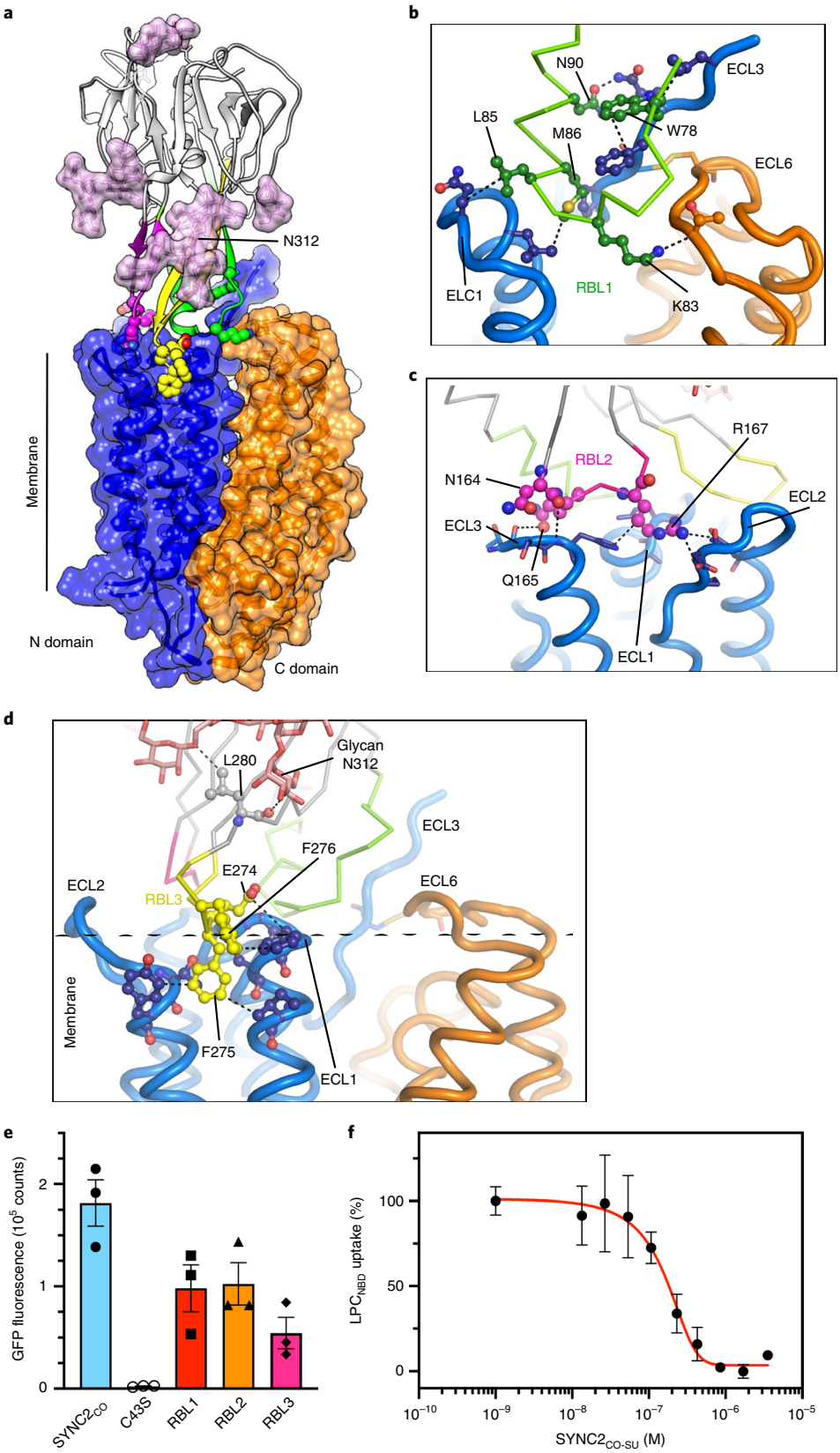

Fig. 4 | SYNC2$_{CO\text{-}SU}$ binding interface and LPC transport inhibition. a, RBL1 (green), RBL2 (pink), and RBL3 (yellow) bind crevices formed between ECLs of MFSD2A$_{CO}$, and are stabilized by N312 glycan and contacts with lipid/detergent molecules within the membrane plane. Glycan molecules are represented as light-pink surfaces. **b**, RBL1 interface. **c**, RBL2 interface. **d**, RBL3 interface. **e**, Fusogenic activity of cells expressing MFSD2A$_{CO}$ and those expressing SYNC2$_{CO}$ or one of the following SYNC2$_{CO}$ mutants: C43S, M86A N90A (RBL1), N164A Q165A (RBL2), or E274A F275A F276A (RBL3). **f**, SYNC2$_{CO\text{-}SU}$ binding abolishes MFSD2A$_{CO}$-mediated uptake of LPC$_{NBD}$. The solid line is the fit of the Hill equation. Plots in **e** and **f** depict the average of three biologically independent experiments, and error bars represent s.e.m. Circles represent values from individual experiments (**e**) or average values (**f**).

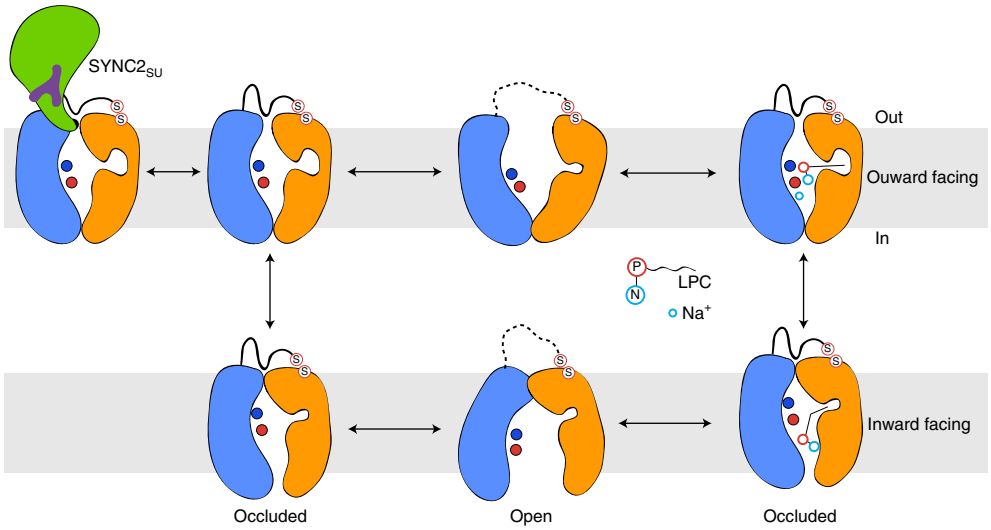

Fig. 5 | MFSD2A transport and SYNC2 allosteric inhibition mechanisms. Cartoon representation of the MFSD2A rock-and-swing transport mechanism and $SYNC2_{SU}$ inhibition. Red and blue solid circles represent D93/E155 and R90/K436 charges, respectively, on the MFSD2A central cavity, while the phosphate (P) and trimethyl-ammonium (N) groups of LPC are represented by empty red and blue circles. Co-transported Na^+ is represented as a smaller empty circle. $SYNC2_{SU}$ (green) trapping a partially-occluded outward-facing state of the cycle is shown, with the N312 glycan in purple.

and isomerization into the inward-facing state. Hence, we hypothesized that SYNC2 binding impairs MFSD2A dynamics and locks the transporter in an outward-facing occluded state, inhibiting transport function.

To experimentally isolate the effect of $SYNC2_{CO\text{-}SU}$ binding on $MFSD2A_{CO}$ transport from other potential effects related to the $SYNC2_{CO\text{-}TM}$ post-fusion transition, we engineered a soluble fragment encompassing the structure of $SYNC2_{CO\text{-}SU}$ and lacking the SYNC2 membrane fusion machinery ($SYNC2_{TM}$). This strategy also enabled an assay of $MFSD2A_{CO}$-mediated substrate uptake in cells in complete absence of detergents or membrane mimetic molecules to maintain transmembrane ionic gradients intact. Strikingly, purified $SYNC2_{CO\text{-}SU}$ abolished Na^+-dependent LPC_{NBD} transport with a half-maximal inhibitory concentration (IC_{50}) of ~200 nM (Fig. 4f), comparable to $SYNC2_{CO}$'s apparent K_D observed in detergent solutions. These results demonstrate that SYNC2 binding inhibits MFSD2A transport function and therefore that MFSD2A receptor and transport molecular mechanisms are intertwined. Notably, they also reveal recombinant $SYNC2_{CO\text{-}SU}$ as a long-sought-after and selective MFSD2A-transport inhibitor that could facilitate delivery of therapeutic molecules through the human BBB.

Discussion

Our structural and functional analyzes of human $MFSD2A_{CO}$–$SYNC2_{CO}$ complex reveal three key molecular aspects of MFSD2A function and pharmacology.

Lipid uptake mechanism across the BBB. We uncovered an outward-facing occluded state of MFSD2A transport cycle displaying a large C-domain cavity, which, in contrast to previous crevices and pockets observed in ortholog structures, is able to accommodate long lipid tails (at least 14 carbons long), and we propose an adapted rocker-switch translocation mechanism that takes up LPC across the BBB (Fig. 5). In this mechanism, outward-facing MFSD2A occludes the LPC headgroup and acyl chain within the transporter. A conserved polar-residue cluster in the central cavity coordinates the LPC headgroup stabilized by counter-charges of R90/K436 and D93/E155. The hydrophobic constriction around F65 'clamps' the lipid tail close to the glycerol moiety, while the bulk of the aliphatic chain is occluded within the C-domain lateral cavity. To adopt such an occluded pose, it is more likely that LPC enters the transporter from the membrane through the TM5/TM8 opening, as suggested by mm-Mfsd2a structural and functional studies[19].

Rotation of N and C domains isomerizes the transporter into the inward-facing state, orienting the central and lateral cavities towards the cytoplasm, as has been observed in the gg-Mfsd2a structure[20]. Upon isomerization, the headgroup of LPC 'swings' from the central-residue cluster into the cytoplasmic side of the transporter before its release, while the acyl chain remains bound to the hydrophobic constriction and lateral cavity. We refer to this as the 'rock-and-swing' mechanism to differentiate it from the classical MFS rocker-switch for smaller-soluble substrates. The rock-and-swing mechanism accounts for the current structural and mutagenesis reported data on MFSD2A and vertebrate orthologs, and expands on the proposed mechanism based on the gg-Mfsd2a structure regarding substrate translocation[20], while opposing the view that the lipid tail remains in the membrane during transport[19].

SYNC2 receptor-recognition mechanism. Highly conserved SYNC2 orthologs are present in all simian species, and constitute a 'fossil' record of what, more than 40 million years ago, was the spike of an exogenous infectious retrovirus with variable receptor-binding determinants[23]. Different mammalian lineages express syncytin envelopes with unrelated receptor usage for placentation, reflecting independent captures of different ancient retroviruses[23,44]. The $MFSD2A–SYNC2_{SU}$ complex represents a 'fossilized' retroviral receptor-recognition mechanism and reveals extensive interactions of the RBLs with non-conserved residues on MFSD2A surface, further stabilized by direct contacts with lipid/detergent molecules and surface glycans. The lack of MFSD2A amino acid conservation at the $SYNC2_{SU}$ binding interface is consistent with independent viral capture across mammalian lineages. In turn, direct interactions of the $SYNC2_{SU}$ RBD with the membrane contrasts with reported receptor-recognition mechanisms of extant human viruses. The RBD of EBOV GP[45] and that of the SARS-CoV-2 spike protein[46], when bound to respective receptors, lay far from the membrane, while that of the human immune deficiency virus (HIV) envelope protein reaches the membrane plane but is shielded from lipids within the co-receptor binding pocket[47].

The involvement of surface glycan molecules in retroviral receptor-mediated fusion mechanisms has been previously observed in HIV[47,48]. Conservation of the SYNC2 'glycan coat' during simian endogenization was likely important to preserve the MFSD2A recognition mechanism and/or the molecular events that trigger the $SYNC2_{TM}$ post-fusion transition upon receptor binding, as suggested by the intimate structural engagement of glycan N312 with the RBD, as well as the inactivating effect of glycosylation-knockout mutants[43].

Therapeutic-drug delivery across the BBB. Neurological and neurodegenerative diseases affecting the central nervous system (CNS) remain a tremendous human health burden[49], and the BBB constitutes a major obstacle to deliver therapeutics into the CNS[50]. MFSD2A has emerged as a potential pharmacological target to overcome that obstacle[18], and our structural and functional results should aid to unleash its pharmacological potential. The structure of outward-facing occluded $MFSD2A_{CO}$ may facilitate rational design of allosteric modulators and/or conjugated substrates with small-compound drugs that bind the ~6,000-$Å^3$ cavity (including central and C-domain lateral chambers) within the transporter. Moreover, we demonstrate that soluble $SYNC2_{CO\text{-}SU}$ inhibits MFSD2A transport function with IC_{50} values in the nanomolar range. This suggests the exciting possibility of using $SYNC2_{CO\text{-}SU}$ to transiently increase vesicular transcytosis across the human BBB endothelium and to aid in delivering therapeutic macromolecules and nano-materials. Further work might be needed to optimize potency and protein stability, and the structure of the $MFSD2A_{CO}$–$SYNC2_{CO\text{-}SU}$ complex should facilitate those efforts.

Online content

Any methods, additional references, Nature Research reporting summaries, source data, extended data, supplementary information, acknowledgements, peer review information; details of author contributions and competing interests; and statements of data and code availability are available at https://doi.org/10.1038/s41594-022-00786-8.

Received: 31 August 2021; Accepted: 1 May 2022;
Published online: 16 June 2022

References

1. Zlokovic, B. V. The blood–brain barrier in health and chronic neurodegenerative disorders. *Neuron* **57**, 178–201 (2008).
2. Chow, B. W. & Gu, C. The molecular constituents of the blood–brain barrier. *Trends Neurosci.* **38**, 598–608 (2015).
3. Nguyen, L. N. et al. Mfsd2a is a transporter for the essential omega-3 fatty acid docosahexaenoic acid. *Nature* **509**, 503–506 (2014).
4. Ben-Zvi, A. et al. Mfsd2a is critical for the formation and function of the blood-brain barrier. *Nature* **509**, 507–511 (2014).
5. Kidd, P. M. Omega-3 DHA and EPA for cognition, behavior, and mood: clinical findings and structural-functional synergies with cell membrane phospholipids. *Alter. Med. Rev.* **12**, 207–227 (2007).
6. Horrocks, L. A. & Yeo, Y. K. Health benefits of docosahexaenoic acid (DHA). *Pharmacol. Res.* **40**, 211–225 (1999).
7. Wong, B. H. et al. Mfsd2a is a transporter for the essential omega-3 fatty acid docosahexaenoic acid (DHA) in eye and is important for photoreceptor cell development. *J. Biol. Chem.* **291**, 10501–10514 (2016).
8. Wong, B. H. & Silver, D. L. Mfsd2a: a physiologically important lysolipid transporter in the brain and eye. *Adv. Exp. Med. Biol.* **1276**, 223–234 (2020).
9. Quek, D. Q., Nguyen, L. N., Fan, H. & Silver, D. L. Structural insights into the transport mechanism of the human sodium-dependent lysophosphatidylcholine transporter MFSD2A. *J. Biol. Chem.* **291**, 9383–9394 (2016).
10. Guemez-Gamboa, A. et al. Inactivating mutations in MFSD2A, required for omega-3 fatty acid transport in brain, cause a lethal microcephaly syndrome. *Nat. Genet.* **47**, 809–813 (2015).
11. Alakbarzade, V. et al. A partially inactivating mutation in the sodium-dependent lysophosphatidylcholine transporter MFSD2A causes a non-lethal microcephaly syndrome. *Nat. Genet.* **47**, 814–817 (2015).
12. Harel, T. et al. Homozygous mutation in MFSD2A, encoding a lysolipid transporter for docosahexanoic acid, is associated with microcephaly and hypomyelination. *Neurogenetics* **19**, 227–235 (2018).
13. Scala, M. et al. Biallelic MFSD2A variants associated with congenital microcephaly, developmental delay, and recognizable neuroimaging features. *Eur. J. Hum. Genet.* **28**, 1509–1519 (2020).
14. Chow, B. W. & Gu, C. Gradual suppression of transcytosis governs functional blood–retinal barrier formation. *Neuron* **93**, 1325–1333 e1323 (2017).
15. Andreone, B. J. et al. Blood–brain barrier permeability is regulated by lipid transport-dependent suppression of caveolae-mediated transcytosis. *Neuron* **94**, 581–594 e585 (2017).
16. O'Brown, N. M., Megason, S. G. & Gu, C. Suppression of transcytosis regulates zebrafish blood–brain barrier function. *eLife* **8**, e47326 (2019).
17. Yang, A. C. et al. Physiological blood–brain transport is impaired with age by a shift in transcytosis. *Nature* **583**, 425–430 (2020).
18. Wang, J. Z. et al. Mfsd2a-based pharmacological strategies for drug delivery across the blood–brain barrier. *Pharmacol. Res.* **104**, 124–131 (2016).
19. Wood, C. A. P. et al. Structure and mechanism of blood-brain-barrier lipid transporter MFSD2A. *Nature* **596**, 444–448 (2021).
20. Cater, R. J. et al. Structural basis of omega-3 fatty acid transport across the blood-brain barrier. *Nature* **595**, 315–319 (2021).
21. Robbins, J. R. & Bakardjiev, A. I. Pathogens and the placental fortress. *Curr. Opin. Microbiol.* **15**, 36–43 (2012).
22. Mi, S. et al. Syncytin is a captive retroviral envelope protein involved in human placental morphogenesis. *Nature* **403**, 785–789 (2000).
23. Blaise, S., de Parseval, N., Benit, L. & Heidmann, T. Genomewide screening for fusogenic human endogenous retrovirus envelopes identifies syncytin 2, a gene conserved on primate evolution. *Proc. Natl Acad. Sci. USA* **100**, 13013–13018 (2003).
24. Mallet, F. et al. The endogenous retroviral locus *ERVWE1* is a bona fide gene involved in hominoid placental physiology. *Proc. Natl Acad. Sci. USA* **101**, 1731–1736 (2004).
25. Roberts, R. M. et al. Syncytins expressed in human placental trophoblast. *Placenta* **113**, 8–14 (2021).
26. Blond, J. L. et al. An envelope glycoprotein of the human endogenous retrovirus HERV-W is expressed in the human placenta and fuses cells expressing the type D mammalian retrovirus receptor. *J. Virol.* **74**, 3321–3329 (2000).
27. Esnault, C. et al. A placenta-specific receptor for the fusogenic, endogenous retrovirus-derived, human syncytin-2. *Proc. Natl Acad. Sci. USA* **105**, 17532–17537 (2008).
28. Rey, F. A. & Lok, S. M. Common features of enveloped viruses and implications for immunogen design for next-generation vaccines. *Cell* **172**, 1319–1334 (2018).
29. Harrison, S. C. Mechanism of membrane fusion by viral envelope proteins. *Adv. Virus Res.* **64**, 231–261 (2005).
30. Chen, C. P. et al. Functional characterization of the human placental fusogenic membrane protein syncytin 2. *Biol. Reprod.* **79**, 815–823 (2008).
31. Renard, M. et al. Crystal structure of a pivotal domain of human syncytin-2, a 40 million years old endogenous retrovirus fusogenic envelope gene captured by primates. *J. Mol. Biol.* **352**, 1029–1034 (2005).
32. Ruigrok, K. et al. X-ray structures of the post-fusion 6-helix bundle of the human syncytins and their functional implications. *J. Mol. Biol.* **431**, 4922–4940 (2019).
33. Cabantous, S., Terwilliger, T. C. & Waldo, G. S. Protein tagging and detection with engineered self-assembling fragments of green fluorescent protein. *Nat. Biotechnol.* **23**, 102–107 (2005).
34. Kumar, A., Planchais, C., Fronzes, R., Mouquet, H. & Reyes, N. Binding mechanisms of therapeutic antibodies to human CD20. *Science* **369**, 793–799 (2020).
35. Vu, T. M. et al. Mfsd2b is essential for the sphingosine-1-phosphate export in erythrocytes and platelets. *Nature* **550**, 524–528 (2017).
36. Kobayashi, N. et al. MFSD2B is a sphingosine 1-phosphate transporter in erythroid cells. *Sci. Rep.* **8**, 4969 (2018).
37. Zhang, B. et al. Structure of a proton-dependent lipid transporter involved in lipoteichoic acids biosynthesis. *Nat. Struct. Mol. Biol.* **27**, 561–569 (2020).
38. Quistgaard, E. M., Low, C., Guettou, F. & Nordlund, P. Understanding transport by the major facilitator superfamily (MFS): structures pave the way. *Nat. Rev. Mol. Cell Biol.* **17**, 123–132 (2016).
39. Yan, N. Structural biology of the major facilitator superfamily transporters. *Annu. Rev. Biophys.* **44**, 257–283 (2015).
40. Holm, L. DALI and the persistence of protein shape. *Protein Sci.* **29**, 128–140 (2020).
41. Varadi, M. et al. AlphaFold protein structure database: massively expanding the structural coverage of protein-sequence space with high-accuracy models. *Nucleic Acids Res.* **50**, D439–D444 (2022).
42. Watanabe, Y. et al. Vulnerabilities in coronavirus glycan shields despite extensive glycosylation. *Nat. Commun.* **11**, 2688 (2020).

43. Cui, L. et al. Effects of individually silenced N-glycosylation sites and non-synonymous single-nucleotide polymorphisms on the fusogenic function of human syncytin-2. *Cell Adh. Migr.* **10**, 39–55 (2016).
44. Lavialle, C. et al. Paleovirology of 'syncytins', retroviral env genes exapted for a role in placentation. *Philos. Trans. R. Soc. Lond. B Biol. Sci.* **368**, 20120507 (2013).
45. Gong, X. et al. Structural INsights Into the Niemann-Pick C1 (NPC1)-mediated cholesterol transfer and Ebola infection. *Cell* **165**, 1467–1478 (2016).
46. Yan, R. et al. Structural basis for the recognition of SARS-CoV-2 by full-length human ACE2. *Science* **367**, 1444–1448 (2020).
47. Shaik, M. M. et al. Structural basis of coreceptor recognition by HIV-1 envelope spike. *Nature* **565**, 318–323 (2019).
48. Ozorowski, G. et al. Open and closed structures reveal allostery and pliability in the HIV-1 envelope spike. *Nature* **547**, 360–363 (2017).
49. GBD 2016 Neurology Collaborators. Global, regional, and national burden of neurological disorders, 1990-2016: a systematic analysis for the Global Burden of Disease Study 2016. *Lancet Neurol.* **18**, 459–480 (2019).
50. Terstappen, G. C., Meyer, A. H., Bell, R. D. & Zhang, W. Strategies for delivering therapeutics across the blood–brain barrier. *Nat. Rev. Drug Discov.* **20**, 362–383 (2021).

Publisher's note Springer Nature remains neutral with regard to jurisdictional claims in published maps and institutional affiliations.

© The Author(s), under exclusive licence to Springer Nature America, Inc. 2022

Methods

Consensus designs and thermal stability assay. Consensus amino acids were calculated using JALVIEW[51] from aligned sequences of representative vertebrate, and simian orthologs of MFSD2A and SYNC2 using Muscle[52]. Criteria to define consensus residues in the alignments were as described before[53]. Consensus amino acid exchanges were simultaneously introduced into wild-type sequences, and in the MFSD2A design care was taken to not introduce exchanges on the predicted extracellular surface of the transporter. As a result, the MFSD2A consensus design shared >96% sequence identity with the wild type and encompasses exchanges at poorly conserved positions mostly within the membrane plane (Extended Data Figs. 1 and 9). Amino acid sequences of SYNC2 simian orthologs are highly conserved and the final consensus design shares ~99% (Extended Data Fig. 8).

Protein expression and purification. Genes encoding MFSD2A constructs were synthesized (GenScript) and subcloned into a pcDNA3.1(+) vector encompassing a N-terminal FLAG-tag, GFP, and PreScission protease cleavage site. Protein expression was done on HEK-293F cells (Thermo Fisher) by transient transfection, as described before[54] with small variations. Briefly, cells grown in FreeStyle 293 medium (Thermo Scientific) were transfected with linear 25K polyethyleneimine (PEI, Polysciences) at a cell density of 2.5×10^6 cells/ml using 3 µg/ml of DNA. Valproic acid (VPA) was added to the culture at a final concentration of 2.2 mM 24 hours after transfection, and cells were grown for additional 24 hours before collection.

Cell pellets were resuspended and lysed in buffer containing: 50 mM HEPES pH 7.4, 200 mM NaCl, 5% vol/vol glycerol, and 1 mM EDTA, and supplemented with protease-inhibitor cocktail (1 mM PMFS, and protease-inhibitor cocktail from Sigma), 1% dodecyl-β-D-Maltopyranoside (DDM, Anatrace), and 0.2% cholesteryl hemi-succinate tris salt (CHS, Anatrace), and incubated for 1 hour. Cell debris was removed by centrifugation in a benchtop centrifuge, and clear supernatants were obtained by ultracentrifugation. Solubilized $MFSD2A_{CO}$ was purified by affinity chromatography using the anti-FLAG M2 affinity gel (Sigma) packed in a gravity column. Resin was pre-equilibrated in buffer A containing 50 mM HEPES pH 7.4, 200 mM NaCl, 5% vol/vol glycerol, 0.03% DDM, and incubated with the transporter for 1 hour under rotation. Resin was extensively washed with buffer A, and the buffer was exchanged to buffer B containing 50 mM HEPES pH 7.4, 200 mM NaCl, 5% vol/vol glycerol, 0.1% glyco-diosgenin (GDN, Anatrace). The protein was eluted in buffer containing 50 mM HEPES pH 7.4, 200 mM NaCl, 5% vol/vol glycerol, 0.0084% GDN, and 100 µg/ml FLAG-peptide (Sigma), and was digested with PreScission protease for 2 hours. Cleaved protein was concentrated to several mg/ml using 100-kDa MWCO concentrator (Corning Spin-X UF concentrators) and injected in a Superose 6 column (GE Healthcare Life Sciences) using a SEC buffer containing 20 mM HEPES pH 7.4, 150 mM NaCl, 5% vol/vol glycerol, 0.0084% GDN. Purified $MFSD2A_{CO}$ was immediately used, or flash frozen and stored at −80 °C. All purification steps were done at 4 °C.

$SYNC2_{CO}$-C43S expression was done using a similar protocol with small modifications. $SYNC2_{CO}$-C43S was synthesized (GenScript) and subcloned into a pcDNA3.1(+) vector encompassing C-terminal PreScission protease cleavage site, GFP, and strep-tag. Protein purification was done as for $MFSD2A_{CO}$ but using StrepTactin resin (GE Healthcare), and elution buffer supplemented with 2.5 mM *d*-desthiobiotin (Sigma). Purified $SYNC2_{CO}$-C43S was kept at 4 °C and used immediately after purification.

For in vitro complexation of $MFSD2A_{CO}$ and $SYNC2_{CO}$-C43S, purified protein samples were mixed and incubated for >1 hour at 4 °C, using threefold molar excess of $SYNC2_{CO}$-C43S over $MFSD2A_{CO}$. Excess $SYNC2_{CO}$-C43S was removed by SEC.

$SYNC2_{CO\text{-}SU}$ was cloned in pcDNA3.1(+) vector with C-terminal EPEA tag, and expressed as secreted protein in HEK-293F. Four days after transfection, culture supernatant was incubated with anti-EPEA tag resin (CaptureSelect C-tagXL Affinity Matrix, Thermo Scientific) for 1 hour at 4 °C, under rotation. Resin was then transferred to a gravity column, and extensively washed with buffer A (50 mM HEPES pH 7.4, 200 mM NaCl, 10% vol/vol glycerol). Protein was eluted with buffer containing 20 mM HEPES pH 7.4, 150 mM NaCl, 5% vol/vol glycerol 2 mM S-E-P-E-A peptide, concentrated using 30 kDa MWCO, and injected into Superose 6 SEC column equilibrated with buffer containing 20 mM HEPES pH 7.4, 150 mM NaCl, 5% vol/vol glycerol.

Purified samples were immediately used or flash frozen and stored at −80 °C.

Thermal stability assay. To assay the effect of consensus mutations on thermal stability, pellets from small-scale cultures (4–8 ml) of transfected cells were resuspended in 800 µl of lysis buffer, dounce homogenized, and lysed by supplementing the buffer with 1% DDM and 0.2% CHS. Samples were under rotation for 1 hour and clear lysates were obtained by ultracentrifugation at 87,000*g* for 40 minutes at 4 °C. Clear lysates were heated at different temperatures for 20 minutes using a PCR thermocycler and ultracentrifuged again (87,000*g*, 50 minutes) to remove precipitates. Samples were assayed in Sepax HPLC column equilibrated with 20 mM HEPES pH 7.4, 150 mM NaCl, 5% glycerol, 0.03% DDM. The output of the column was connected to a fluorimeter (Quanta Master, HORIBA) to quantify elution profiles.

Cell fusion assays. The cell fusion assay was based on split-GFP complementation system[33]. GFP β-strand 11 (GFP_{11}) was fused to the C terminus of MFSD2A using a previously reported strategy[55], while a gene encoding GFP β-strands 1–10 (GFP_{1-10}) was cloned in pcDNA3.1(+) vector.

HEK-293T.17 (ATCC) adherent cells were grown in DMEM medium (Gibco) supplemented with 10% heat-inactivated fetal bovine serum (FBS, GE Healthcare Life Sciences), penicillin–streptomycin antibiotics (100 units/ml penicillin and 100 µg/ml streptomycin, Gibco), glutamine (2 mM), and minimum essential medium non-essential amino acids (1× MEM NEAA, Gibco). Cells cultured in 24-well plates were transfected with MFSD2A-GFP_{11} plasmid, or co-transfected with SYNC2 (WT or mutants) plus GFP_{1-10} plasmids, respectively, using lipofectamine 2000 (Invitrogen), and following manufacturer recommendations. Twenty-four hours after transfections, cells were gently washed with PBS, and those expressing SYNC2-GFP_{1-10} (or mutants) were resuspended and layered over attached cells expressing MFSD2A-GFP_{11}, and incubated at 37 °C for nearly 3 hours. Then, cells were detached, transferred to Eppendorf tubes, washed with PBS by centrifugation, and finally transferred to a 96-well plate for fluorescence quantification. GFP fluorescence was measured using CLARIOstar-Plus plate reader (BMG Labtech; $\lambda_{excitation} = 470$ nm and $\lambda_{emission} = 514$ nm). Three biologically independent experiments were quantified in triplicate samples.

LPC-analog transport assay. Sodium-dependent substrate uptake was measured in HEK-293T.17 cells, grown and transfected as described above. Twenty-four hours after transfection, cells were washed with pre-warmed PBS, and ~1 million cells were pelleted and resuspended in 500 µl of transport buffer (20 mM HEPES pH 7.4, 150 mM NaCl, 1.7 mM KCl, 1.2 mM $MgCl_2$, 2.5 mM $CaCl_2$, 5 mM Glc). MFSD2A substrate analog LPC_{NBD} (Avanti Polar Lipids) was added to indicated final concentrations from 5 mM DMSO stock, and cells were incubated for 10 minutes at 37 °C. The ligand excess was removed by centrifugation, and cells were resuspended in 200 µl of PBS and transferred to black 96-well flat-bottom plates (grenier). Fluorescence quantification was done in a microplate reader (CLARIOstar-Plus) using $\lambda_{excitation} = 464$ nm and $\lambda_{emission} = 531$ nm. Three biologically independent experiments were quantified in triplicate samples. LPC_{NBD} titration of transport was fitted to Hill-like equation using Prism (GraphPad)

To probe the effect of $SYNC2_{CO\text{-}SU}$ on $MFSD2A_{CO}$ function, cells were incubated with purified $SYNC2_{CO\text{-}SU}$ at different concentrations for 10 minutes at 37 °C, before assaying transport using of 20 µM LPC_{NBD}. Transport inhibition data were fitted to Hill-like equation using Prism (GraphPad).

Confocal microscopy imaging. Cells were transfected as described above for the transport assay with GFP (N-terminal) fusion constructs of MFSD2A (GFP-MFSD2A). Twenty-four hours after transfection, live cells were imaged in an inverted Leica SP8 confocal system equipped with temperature-controlled chamber and using a ×93/1.30 GLYC CORR objective (Leica).

SYNC2 binding assay in detergent solutions. $SYNC2_{CO}$ binding to $MFSD2A_{CO}$ was assayed in clear lysates of detergent-solubilized HEK-293F cells expressing mCherry (C-terminal) and GFP (N-terminal) fusion constructs of $SYNC2_{CO}$ and $MFSD2A_{CO}$, respectively, that enable protein quantification. Clear cells lysates were obtained by 1-hour solubilization in lysis buffer containing 50 mM HEPES pH 7.4, 200 mM NaCl, 5% vol/vol glycerol, 1 mM EDTA, protease-inhibitor cocktail, 1% DDM, and 0.2% CHS, followed by centrifugation (3,800*g*, 20 min). $SYNC2_{CO}$-mCherry and GFP-$MFSD2A_{CO}$ protein concentrations in lysates were determined using purified standards in a microplate reader (CLARIOstar-Plus) set at 570/620 and 470/514 ($\lambda_{excitation}/\lambda_{emission}$), respectively. GFP-$MFSD2A_{CO}$ lysate at 500 nM was incubated with 2 ml anti-FLAG M2 resin for 1 hour, fractionated in 8 equal parts placed on gravity columns and washed with 1 ml of wash buffer (50 mM HEPES pH 7.4, 200 mM NaCl, 5% vol/vol glycerol, 0.03% DDM, and 0.006% CHS). $SYNC2_{CO}$-mCherry was added from a calibrated stock at 2 µM, and equilibrated for 1 hour. Unbound $SYNC2_{CO}$-mCherry was removed with wash buffer, and samples were eluted with buffer containing: 20 mM HEPES pH 7.4, 150 mM NaCl, 5% vol/vol glycerol, 0.03% DDM, 0.006% CHS, and 100 µg/ml FLAG peptide. All binding steps were done at 4 °C. Eluted protein was transferred to a 96-well flat-bottom black plate for quantification of GFP and mCherry fluorescence. $SYNC2_{CO}$-mCherry fluorescence background was determined from samples with anti-FLAG resin that lack GFP-$MFSD2A_{CO}$ bound. $SYNC2_{CO}$-mCherry subtracted fluorescence was fitted to a quadratic binding equation using Sigma Plot (Systat):

$$Y = \left(\frac{([M] + [S] + KD) - \sqrt{(-([M] + [S] + KD))^2 - 4[M][S]}}{2} \right) / [M]$$

Where Y is the fraction of $SYNC2_{CO}$-mCherry bound to GFP-$MFSD2A_{CO}$, K_D is the apparent dissociation binding constant, and $[M]$ and $[S]$ are total GFP-$MFSD2A_{CO}$ and $SYNC2_{CO}$-mCherry concentrations, respectively.

Electron microscopy sample preparation and data acquisition. $MFSD2A_{CO}$–$SYNC2_{CO}$ purified complex was applied to glow-discharged Au 200 mesh Quantifoil R1.2/ 1.3 holey carbon grids (Quantifoil), and vitrified using Vitrobot Mark IV (Thermo Fisher). Typically, 4 µl of sample at 1.2–1.5 mg/ml were applied

to the grids, and the Vitrobot chamber was maintained at 100% humidity and 4 °C. Grids were screened in 200 keV Talos Arctica microscope (Thermo Fisher) at the IECB cryo-EM imaging facility. Data collection was performed with a 300 keV Titan Krios microscope (ThermoFisher) at EMBL-Heidelberg Cryo-Electron Microscopy Service Platform, equipped with a K2 direct electron detector (Gatan). Images were recorded with SerialEM[56] at ×105,000x corresponding to a pixel size of 0.814 Å. Dose rate was 3 electrons/pixel/s, and the defocus range was −0.5 to −1.8 µm. Images were collected for 8 s with 0.2-s subframes (total 40 subframes), corresponding to a total dose of 47 electrons/Å^2. In total, 7,365 movies were recorded.

Cryo-EM data processing, model building, and structure analysis. All data sets were processed with cryoSPARC v2 (ref. [57]). Movies were gain corrected and aligned using in-built patch-motion correction routine. CTF parameters were estimated using in-built patch-CTF routine in cryoSPARC. Low-quality images were discarded automatically by setting a CTF-resolution threshold of 20 Å, as well as manually upon visual inspection. About 2,000 particles were manually picked and were used to generated 2D templates for autopicking, and this process was iterated several times. Then, 1,461,938 auto-picked particles were 4× Fourier cropped and initially subjected to rounds of 2D classification, followed by ab initio classification. Ab initio volumes displaying secondary structural elements of MFSD2A$_{CO}$ and SYNC2$_{CO}$ were then used to re-classify the entire set of auto-picked particles (4× Fourier cropped) using rounds of heterogeneous refinement. We also included ab initio volumes without molecular features to generate 'bad' classes. Next, 199,300 selected particles were re-extracted without Fourier cropping and used for ab initio reconstruction and non-uniform refinement[58] that yielded a ~4-Å map. Further focused refinement masking out the detergent micelle yielded a final map at an overall 3.6-Å resolution, based on the 'gold-standard' 0.143 FSC cut-off that was used for model building (EMDB-12935). In order to improve density corresponding to glycans and some surface loops, a second map with a slightly softer mask was calculated (overall ~3.8-Å resolution), and was used to aid model building of such regions. This secondary map is available as part of the EMDB-12935 entry. Maps were visualized and analyzed using UCSF Chimera[59] and sharpened with phenix.autosharpen in PHENIX[60].

The MFSD2A$_{CO}$–SYNC2$_{CO\text{-}SU}$ structure was built de novo using Coot[61]. Secondary-structure predictions using JPred[62] and XtalPred-RF[63] were used to help initial sequence assignment. Atomic coordinates were refined using PHENIX[64]. The SYNC2$_{CO\text{-}SU}$ model includes residues Y58–V322, and the MFSD2A$_{CO}$ model includes 44–217 and 233–509. The cryo-EM map was in general weaker in some distal parts of SYNC2$_{CO\text{-}SU}$ from MFSD2A$_{CO}$ (SYNC2$_{CO\text{-}SU}$), as well as in exposed loops of the transporter connecting TMs. Owing to this, we were not able to completely build ECL3 loop, or unambiguously assign the position of all residues in other loops (MFSD2A$_{CO}$ ECL5 and interdomain loop; SYNC2$_{CO}$ F114–L120, L186–K198, and S223–E226). In general, the secondary map mentioned above was used to help build these regions.

Structural analyses were carried out as follows: protein cavity calculations with CASTp 3.0 (ref. [65]). The volumes reported in the text are molecular surface volumes calculated with a default 1.4-Å-radius probe. The cavities displayed in Extended Data Fig. 6 were calculated with a 2.0-Å-radius probe to match the methyl-group VDW radius. Protein–protein interfaces with PISA[66], structural alignments and structural homology PDB search with DALI[40], and amino acid conservation surface mapping with ConSurf[67]. Docking of LPC 18:3 into MFSD2A$_{CO}$ structure was done with HADDOCK 2.4 server using 'EASY' access level with default parameters, and the following list of active residues: 56, 60, 61, 65, 90, 93, 151, 155, 436, 309, 311, 312, 313, 315, 318, 319, 332, 333, 336, 371, 373, 374, 387, 388, 391, 474, and 475.

Reporting summary. Further information on research design is available in the Nature Research Reporting Summary linked to this article.

Data availability

The structural model of the MFSD2A$_{CO}$–SYNC2$_{CO}$ complex has been deposited in the Protein Data Bank under accession code 7OIX, and associated cryo-EM maps were deposited in the Electron Microscopy Data Bank (EMDB) under accession number EMD-12935. Materials are available upon reasonable request. Source data are provided with this paper.

References

51. Waterhouse, A. M., Procter, J. B., Martin, D. M., Clamp, M. & Barton, G.J. Jalview Version 2—a multiple sequence alignment editor and analysis workbench. *Bioinformatics* **25**, 1189–1191 (2009).
52. Edgar, R. C. MUSCLE: multiple sequence alignment with high accuracy and high throughput. *Nucleic Acids Res.* **32**, 1792–1797 (2004).
53. Cirri, E. et al. Consensus designs and thermal stability determinants of a human glutamate transporter. *eLife* **7**, e40110 (2018)
54. Canul-Tec, J. C. et al. Structure and allosteric inhibition of excitatory amino acid transporter 1. *Nature* **544**, 446–451 (2017).
55. Kaddoum, L., Magdeleine, E., Waldo, G. S., Joly, E. & Cabantous, S. One-step split GFP staining for sensitive protein detection and localization in mammalian cells. *Biotechniques* **49**, 727–736 (2010).
56. Mastronarde, D. N. Automated electron microscope tomography using robust prediction of specimen movements. *J. Struct. Biol.* **152**, 36–51 (2005).
57. Punjani, A., Rubinstein, J. L., Fleet, D. J. & Brubaker, M. A. cryoSPARC: algorithms for rapid unsupervised cryo-EM structure determination. *Nat. Methods* **14**, 290–296 (2017).
58. Punjani, A., Zhang, H. & Fleet, D. J. Non-uniform refinement: adaptive regularization improves single-particle cryo-EM reconstruction. *Nat. Methods* **17**, 1214–1221 (2020).
59. Pettersen, E. F. et al. UCSF Chimera—a visualization system for exploratory research and analysis. *J. Comput. Chem.* **25**, 1605–1612 (2004).
60. Terwilliger, T. C., Sobolev, O. V., Afonine, P. V. & Adams, P. D. Automated map sharpening by maximization of detail and connectivity. *Acta Crystallogr D. Struct. Biol.* **74**, 545–559 (2018).
61. Emsley, P., Lohkamp, B., Scott, W. G. & Cowtan, K. Features and development of Coot. *Acta. Crystallogr. D. Biol. Crystallogr.* **66**, 486–501 (2010).
62. Drozdetskiy, A., Cole, C., Procter, J. & Barton, G. J. JPred4: a protein secondary structure prediction server. *Nucleic Acids Res.* **43**, W389–W394 (2015).
63. Slabinski, L. et al. XtalPred: a web server for prediction of protein crystallizability. *Bioinformatics* **23**, 3403–3405 (2007).
64. Adams, P. D. et al. PHENIX: a comprehensive Python-based system for macromolecular structure solution. *Acta Crystallogr. D. Biol. Crystallogr.* **66**, 213–221 (2010).
65. Tian, W., Chen, C., Lei, X., Zhao, J. & Liang, J. CASTp 3.0: computed atlas of surface topography of proteins. *Nucleic Acids Res.* **46**, W363–W367 (2018).
66. Krissinel, E. & Henrick, K. Inference of macromolecular assemblies from crystalline state. *J. Mol. Biol.* **372**, 774–797 (2007).
67. Glaser, F. et al. ConSurf: identification of functional regions in proteins by surface-mapping of phylogenetic information. *Bioinformatics* **19**, 163–164 (2003).

Acknowledgements

The IECB cryo-EM imaging facility (Pessac) is acknowledged for support in cryo-EM sample screening and initial data acquisition, and EMBL-Heidelberg Cryo-Electron Microscopy Service Platform for support in image acquisition. Confocal-microscopy image acquisition was done by the Bordeaux Imaging Center that is supported by the French National Research Agency (ANR-10-INSB-04). This research was funded by the European Research Council (ERC) under European Union Horizon 2020 Program (Grant 771965), IDEX Senior Chair of Bordeaux University, and Region Nouvelle-Aquitaine (Grant 8166910) to N. R.

Author contributions

M. M.-M. optimized and performed protein expression, purification, functional assays, cryo-EM sample preparation, and data collection, as well as atomic model building and refinement. E. N. performed transport assays and prepared samples for confocal imaging. M. M.-M. and N. R. analyzed cryo-EM data, functional data, and structure, as well as prepared the manuscript. N. R. conceived and supervised the project.

Competing interests

M.M-M. and N.R. are co-inventors in a patent application (63/316,885) by Institut Pasteur related to SYNC2 constructs used in this work.

Additional information

Extended data is available for this paper at https://doi.org/10.1038/s41594-022-00786-8.

Supplementary information The online version contains supplementary material available at https://doi.org/10.1038/s41594-022-00786-8.

Correspondence and requests for materials should be addressed to Nicolas Reyes.

Peer review information *Nature Structural and Molecular Biology* thanks Markus Seeger and Robert Stahlin for their contribution to the peer review of this work. Beth Moorefield was the primary editor on this article and managed its editorial process and peer review in collaboration with the rest of the editorial team. Peer reviewer reports are available.

Reprints and permissions information is available at www.nature.com/reprints.

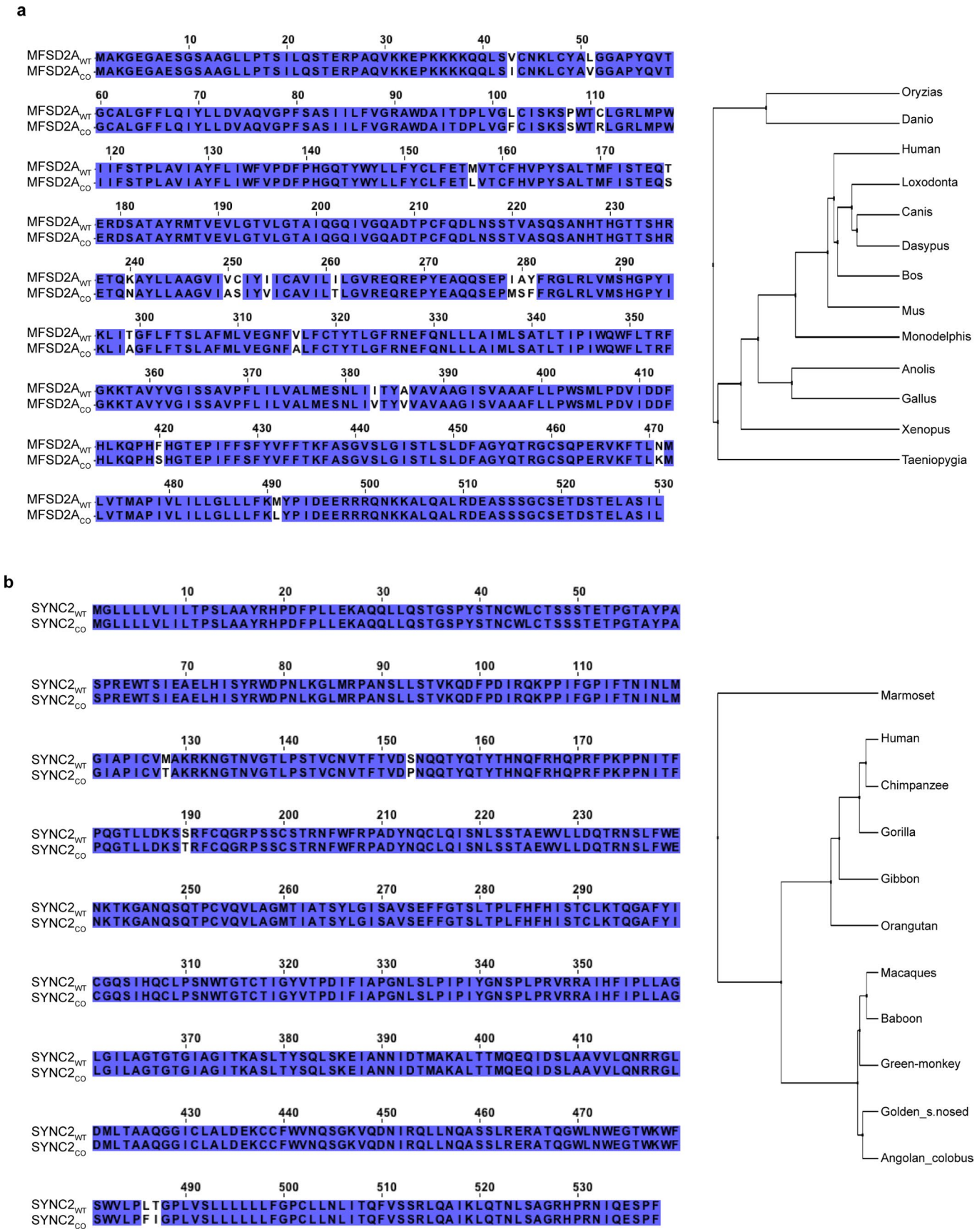

Extended Data Fig. 1 | Consensus designs. a, Phylogenetic tree of MFSD2A vertebrate orthologs used to calculate consensus amino acids, and amino acid sequence alignment of human MFSD2A$_{WT}$ and MFSD2A$_{CO}$. **b**, Phylogenetic tree of SYNC2$_{CO}$ simian orthologs used to calculate consensus amino acids, and amino acid sequence alignment of human SYNC2$_{WT}$ and SYNC2$_{CO}$.

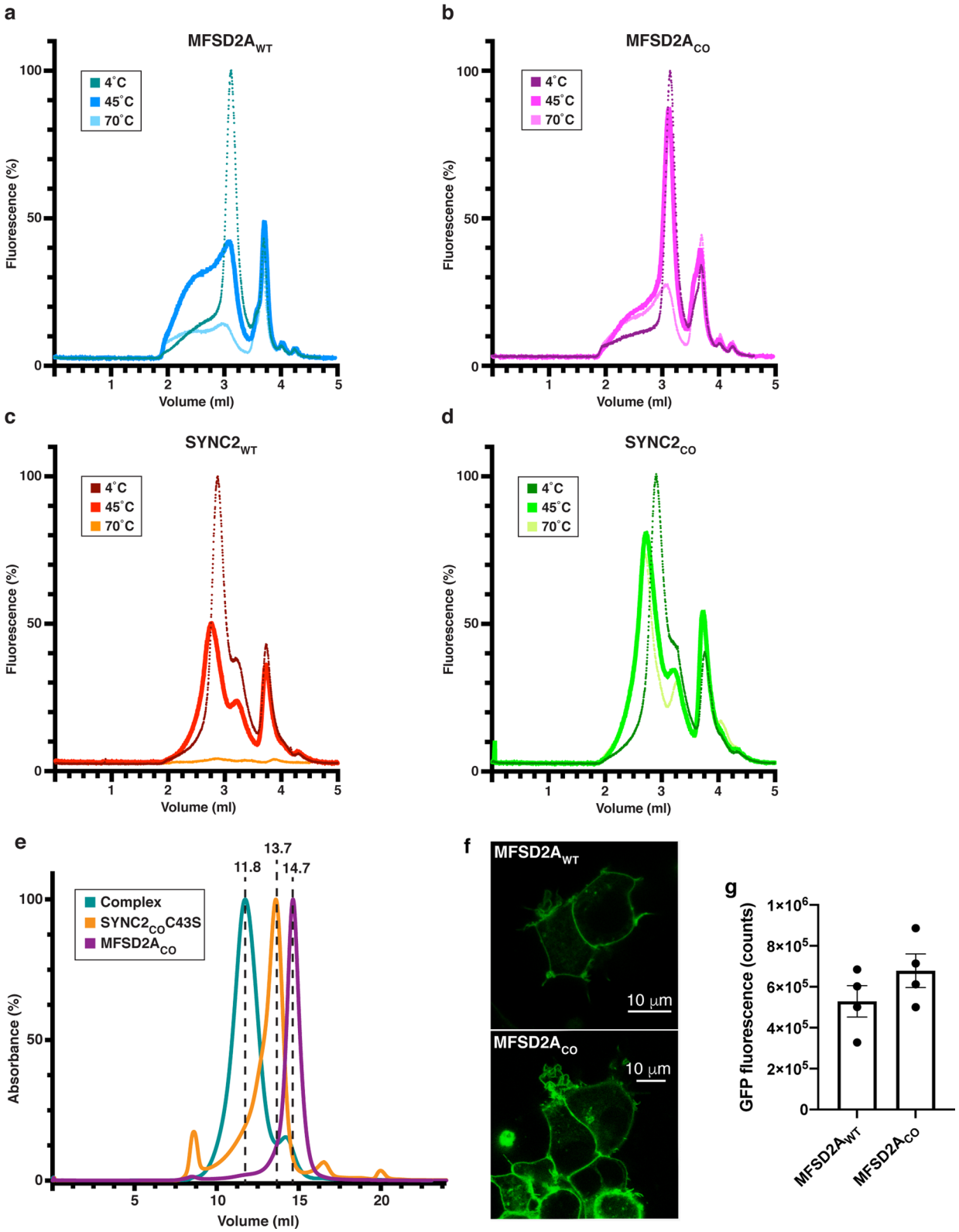

Extended Data Fig. 2 | Thermal-stability and cell-expression of wild-type and consensus designs. Detergent solubilized protein samples were pre-heated at 4, 45 and 70˚C, and assayed by fluorescence-based SEC. Traces corresponding to samples pre-heated at 45˚C are highlighted for comparison. **a**, MFSD2A$_{WT}$. **b**, MFSD2A consensus design. **c**, SYNC2$_{WT}$. **d**, SYNC2 consensus design. **e**, Representative SEC traces of purified MFSD2A$_{CO}$, SYNC2$_{CO}$-C43S, and MFSD2A$_{CO}$:SYNC2$_{CO}$-C43S complex, respectively, with the corresponding elution volumes in a Superose 6 SEC column (24 ml bed volume). **f**, Confocal images of cells expressing MFSD2A$_{WT}$ and MFSD2A$_{CO}$ GFP fusion constructs. **g**, Total GFP fluorescence (quantified in a microplate reader) of cells expressing MFSD2A$_{WT}$ and MFSD2A$_{CO}$ GFP fusion constructs. Plots depict average of three biologically independent experiments, and error bars represent s.e.m.

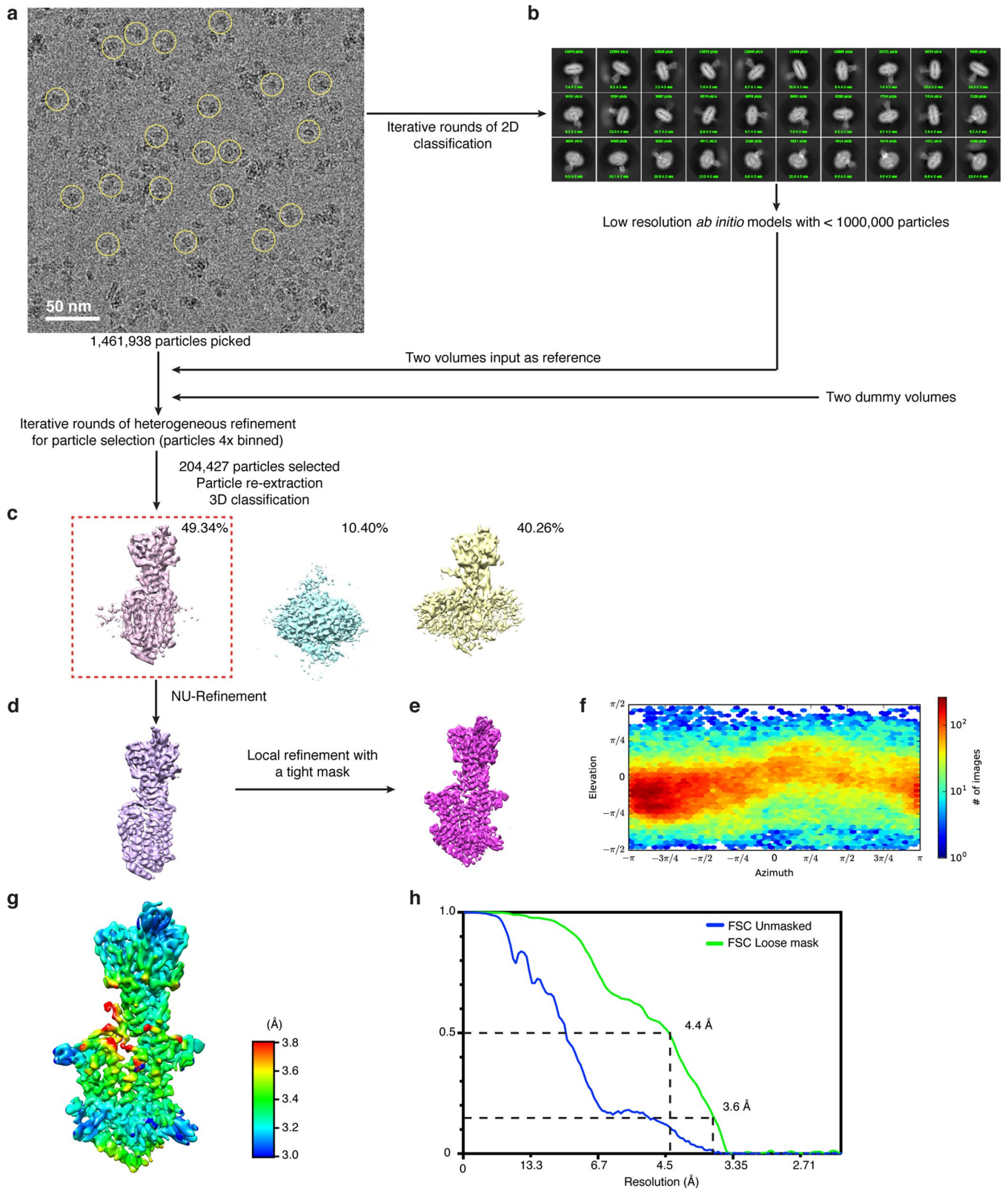

Extended Data Fig. 3 | Cryo-EM data processing pipeline. a, Representative EM micrograph. 7,365 micrographs were collected **b**, Gallery of representative 2D class-averages. **c**, 3D classes from heterogenous refinement. **d**, Non-uniform refinement 3D map. **e**, Local-refinement map after micelle removal. **f**, Viewing direction distribution plot. **g**, Color coded map according to local resolution estimation. **h**, Fourier shell correlation (FSC) plot of local refinement with FSC thresholds at 0.143 and 0.5.

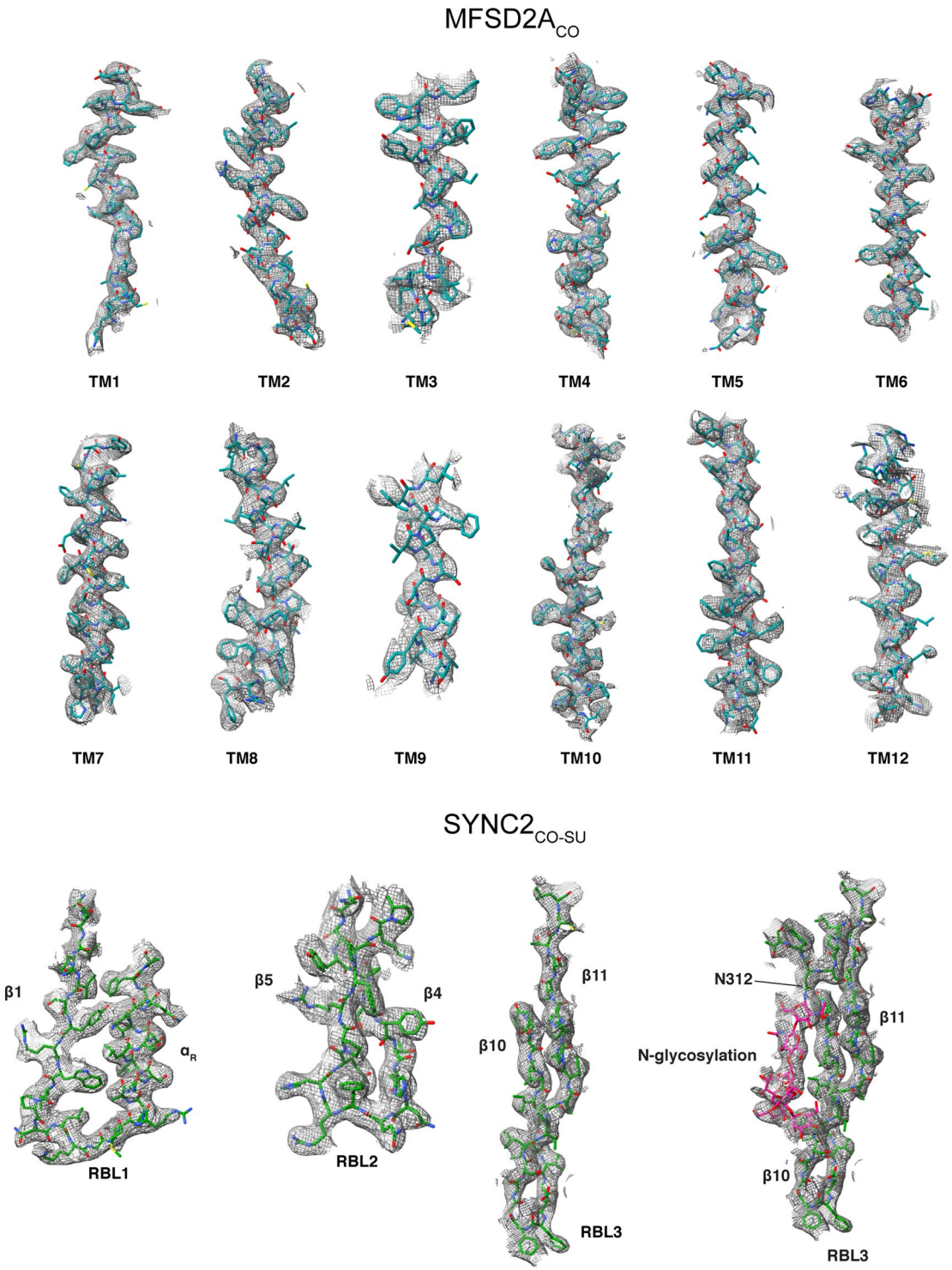

Extended Data Fig. 4 | EM density in MFSD2A$_{CO}$:SYNC2$_{CO-SU}$ complex structure. Cryo-EM density corresponding to representative individual structural elements of MFSD2A$_{CO}$ and SYNC2$_{CO}$-SU.

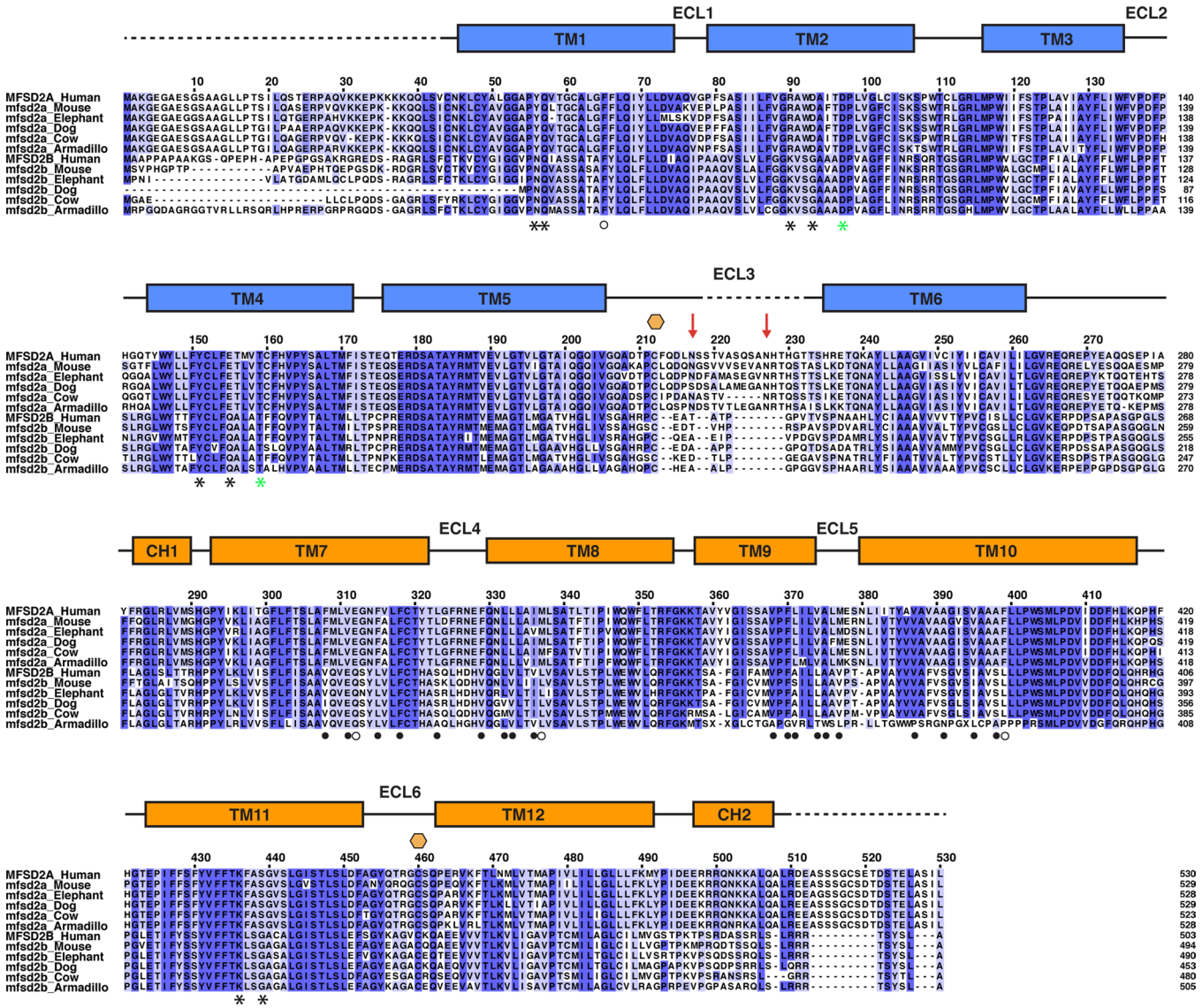

Extended Data Fig. 5 | Amino acid sequence alignment of MFSD2A and MFSD2B mammalian orthologs. Asterisks indicate the position of MFSD2A conserved residues that potentially contribute to LPC (black) and Na^+ (green) coordination in the central cavity. Solid circles indicate conserved residues facing the lateral cavity, and empty circles those at the constriction. Yellow polygons indicate cysteine residues involved in ECL3-ECL6 disulfide bond. Dashed lines indicate MFSD2A regions that were not modeled in the structure, and red arrows potential N-glycosylation sites on MFSD2A.

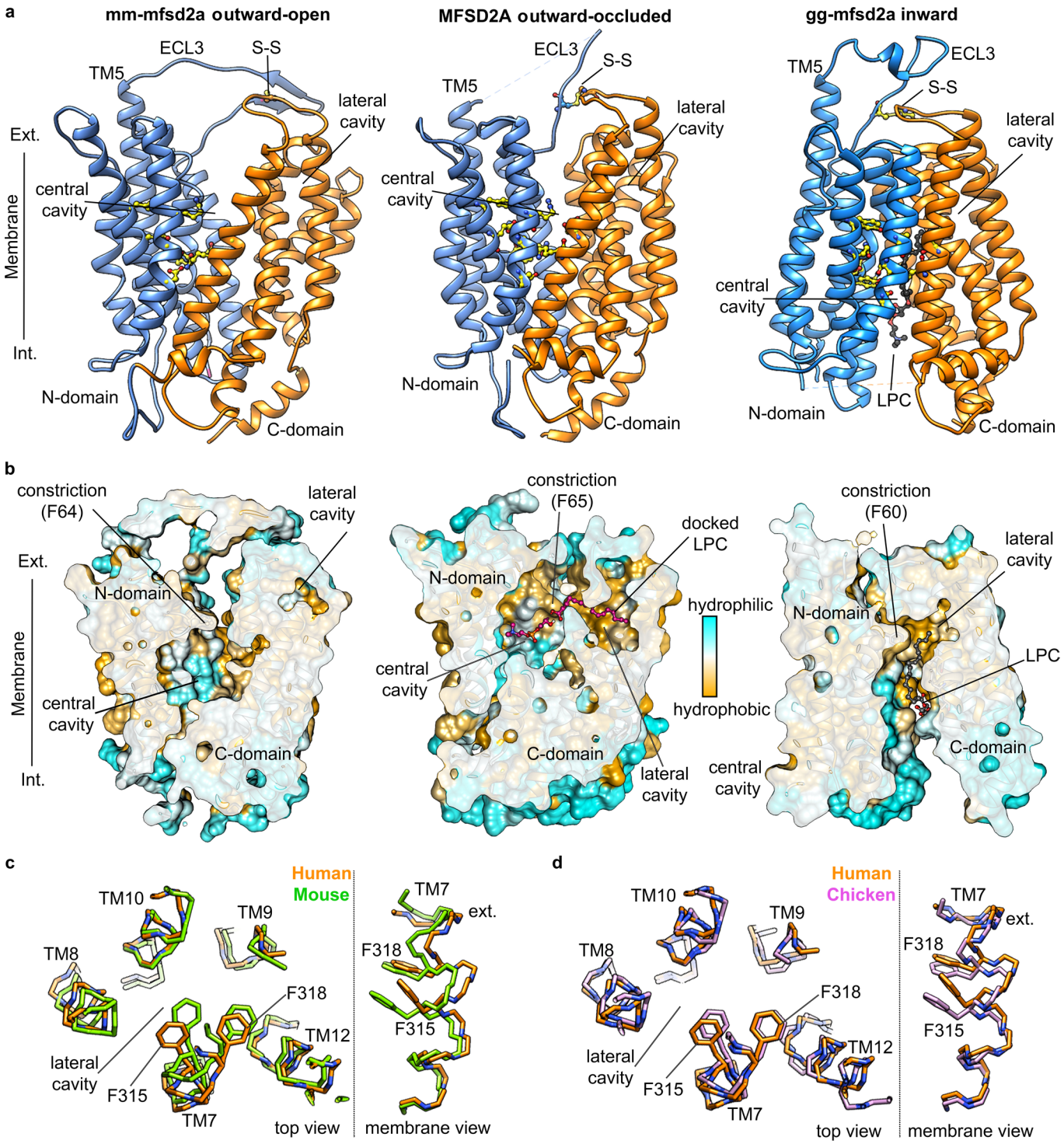

Extended Data Fig. 6 | Structural comparison of MFSD2A$_{co}$ and vertebrate orthologs. Cartoon representations of outward-open (mouse mfsd2A; PDB 7N98), outward-occluded (this work), and inward-open (chicken mfsd2a; PDB 7MJS) structures. **b**, Corresponding molecular surface representations colored by residue hydrophobicity. Central and lateral cavities are highlighted. MFSD2A$_{co}$ surface with docked LPC is also shown in Fig. 2c. **c**, Structural alignment of MFSD2A$_{co}$ (orange) and mm-mfsd2a (green) C-domains. **d**, Structural alignment of MFSD2A$_{co}$ (orange) and gg-mfsd2a (light-pink) C-domains.

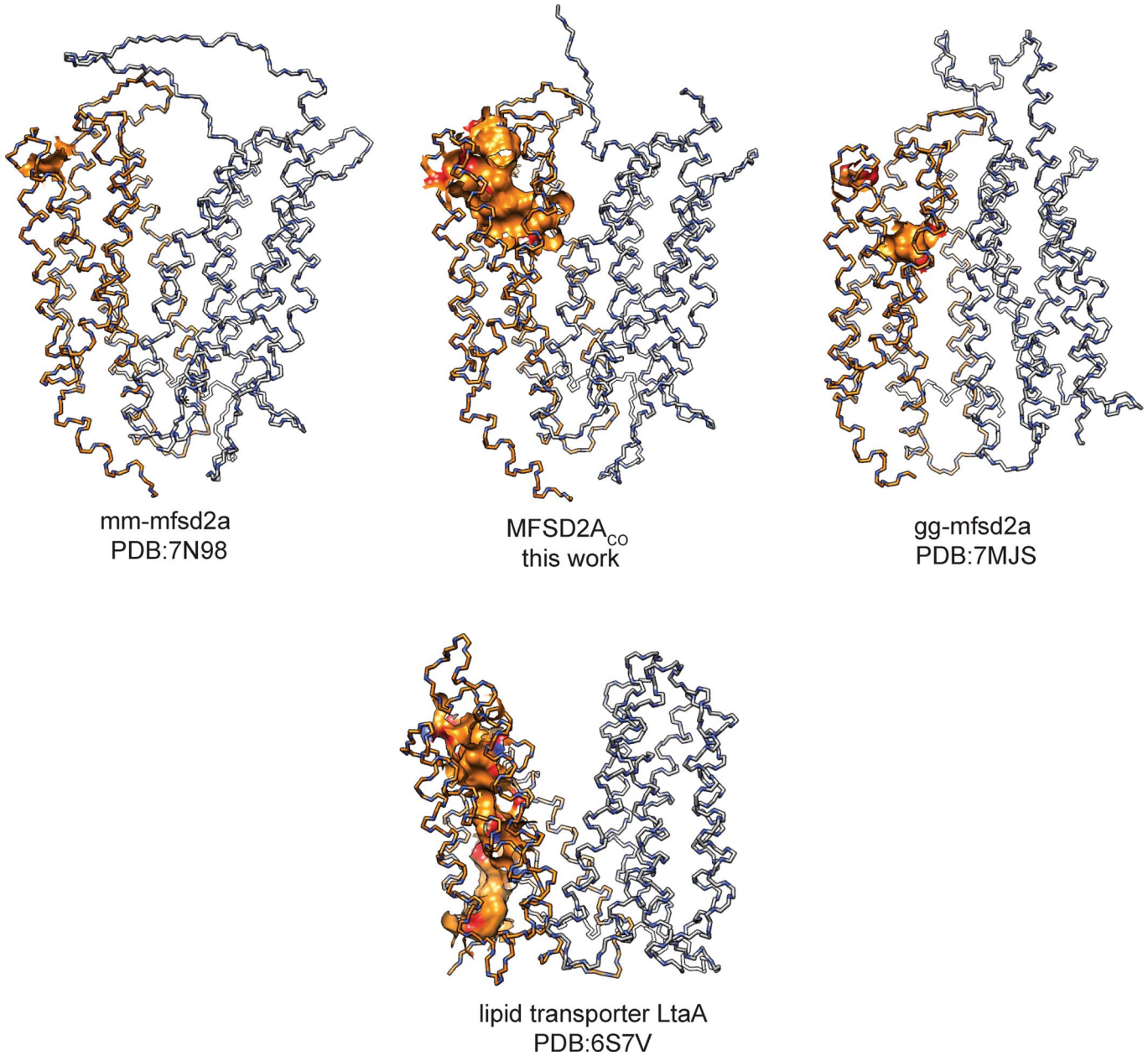

Extended Data Fig. 7 | C-domain cavities in MFS lipid transporters. Transporters are represented with C-domain (orange) to the left, and N-domain (grey) to the right. Cavity surface in the C-domain was calculated with CASTp 3.0 using a 2-angstrom radius probe, corresponding to the methyl-group VWD radius, and otherwise default parameters.

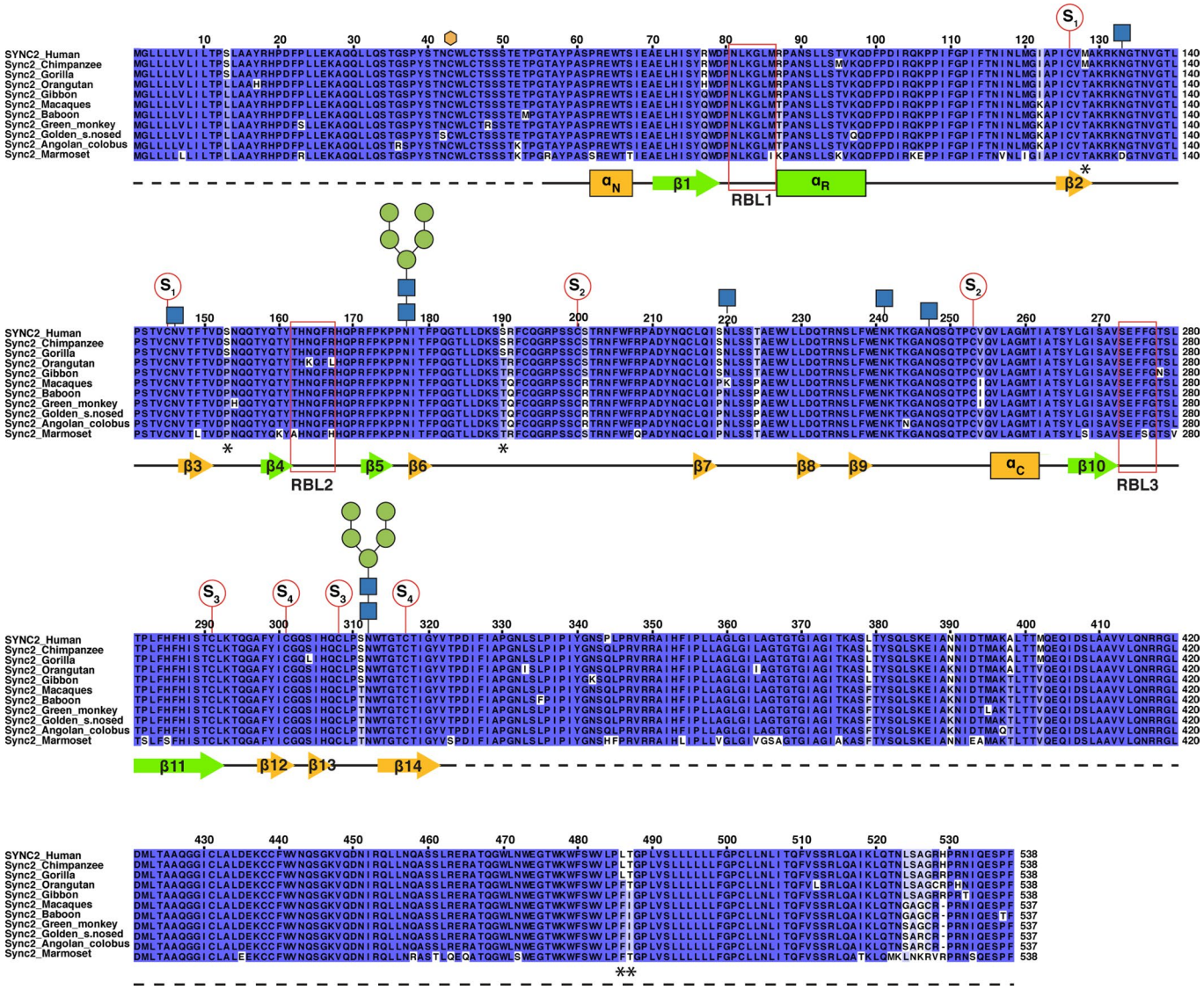

Extended Data Fig. 8 | Amino acid sequence alignment of SYNC2 simian orthologs. Disulfide bonds are indicated by red circles and numbered as follows: S_1 corresponds to disulfide C126-C145, S_2 to C200-C253, S_3 to C291-C308, and S_4 to C301-C317. Glycan molecules are represented over corresponding asparagine residues with N-Acetylglucosamine (blue square), and mannose (green circle) residues indicated. Receptor binding loops (RBLs) are framed in red squares. In SYNC2 consensus design the following exchanges were introduced: M128T, S153P, S190T, L486F and T487I (asterisks).

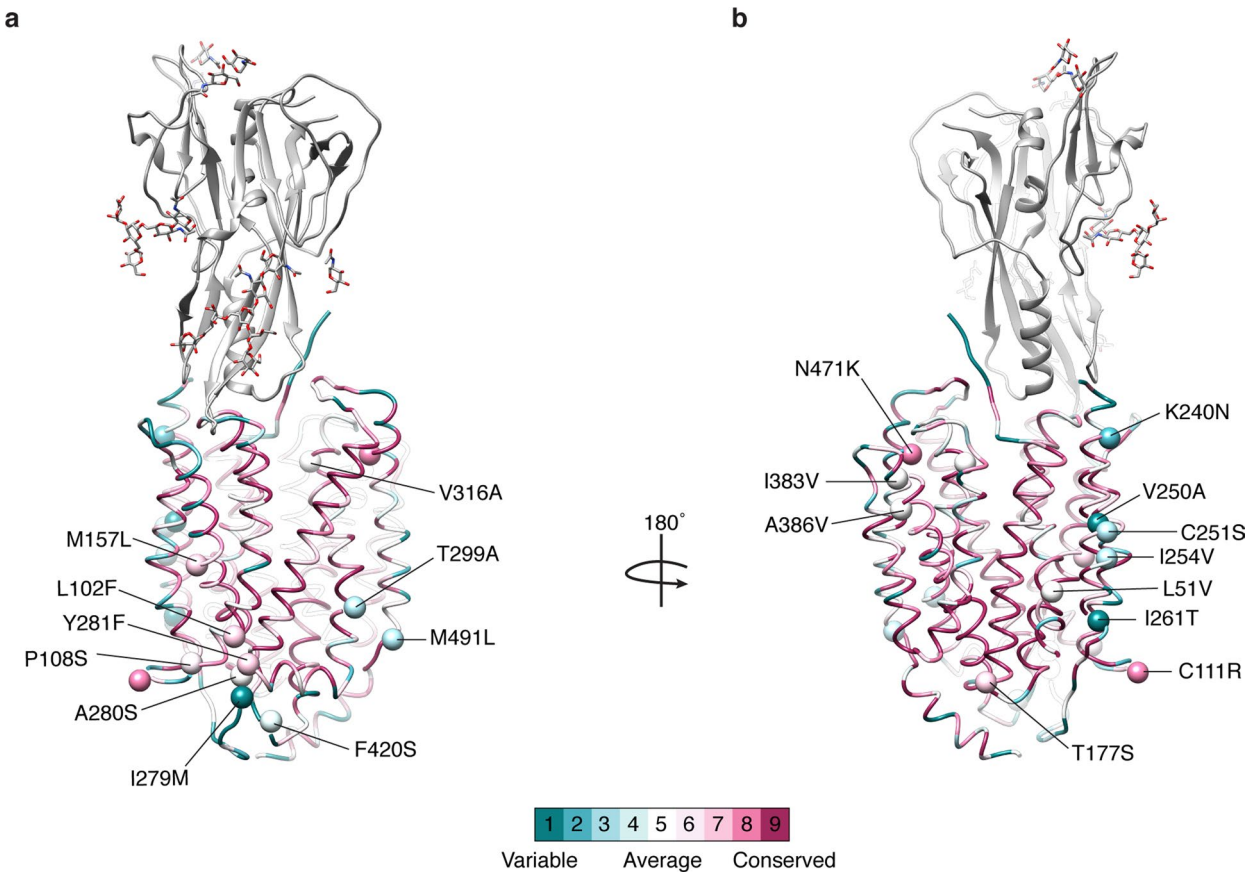

Extended Data Fig. 9 | MFSD2A amino-acid conservation surface mapping. Amino acid conservation across MFSD2A vertebrate orthologs is mapped into the structure of $MFSD2A_{CO}$:$SYNC2_{CO}$-SU complex. $SYNC2_{CO}$-SU is shown in gray and binds to poorly-conserved residues on the extracellular surface of $MFSD2A_{CO}$. Spheres represent alpha-carbon atoms of consensus exchanges introduced in $MFSD2A_{WT}$ to improve thermal stability.

nature portfolio

Corresponding author(s): Nicolas Reyes

Last updated by author(s): Apr 6, 2022

Reporting Summary

Nature Portfolio wishes to improve the reproducibility of the work that we publish. This form provides structure for consistency and transparency in reporting. For further information on Nature Portfolio policies, see our Editorial Policies and the Editorial Policy Checklist.

Statistics

For all statistical analyses, confirm that the following items are present in the figure legend, table legend, main text, or Methods section.

n/a	Confirmed
☐	☒ The exact sample size (*n*) for each experimental group/condition, given as a discrete number and unit of measurement
☐	☒ A statement on whether measurements were taken from distinct samples or whether the same sample was measured repeatedly
☒	☐ The statistical test(s) used AND whether they are one- or two-sided *Only common tests should be described solely by name; describe more complex techniques in the Methods section.*
☒	☐ A description of all covariates tested
☒	☐ A description of any assumptions or corrections, such as tests of normality and adjustment for multiple comparisons
☐	☒ A full description of the statistical parameters including central tendency (e.g. means) or other basic estimates (e.g. regression coefficient) AND variation (e.g. standard deviation) or associated estimates of uncertainty (e.g. confidence intervals)
☒	☐ For null hypothesis testing, the test statistic (e.g. *F*, *t*, *r*) with confidence intervals, effect sizes, degrees of freedom and *P* value noted *Give P values as exact values whenever suitable.*
☒	☐ For Bayesian analysis, information on the choice of priors and Markov chain Monte Carlo settings
☒	☐ For hierarchical and complex designs, identification of the appropriate level for tests and full reporting of outcomes
☒	☐ Estimates of effect sizes (e.g. Cohen's *d*, Pearson's *r*), indicating how they were calculated

Our web collection on statistics for biologists contains articles on many of the points above.

Software and code

Policy information about availability of computer code

Data collection	SerialEM 3.8.16
Data analysis	cryoSPARC v2 , USF Chimera 1.14, COOT 0.8.9.2, Prism 8.0.1, SigmaPlot 12, Jalview 2.10.4b1, Phenix 1.18.2, CASTp 3.0, PISA 1.52, Consurf 2016, Muscle 3.8.31, Jred 4, XtalPred-RF, HADDOCK 2.4

For manuscripts utilizing custom algorithms or software that are central to the research but not yet described in published literature, software must be made available to editors and reviewers. We strongly encourage code deposition in a community repository (e.g. GitHub). See the Nature Portfolio guidelines for submitting code & software for further information.

Data

Policy information about availability of data

All manuscripts must include a data availability statement. This statement should provide the following information, where applicable:

- Accession codes, unique identifiers, or web links for publicly available datasets
- A description of any restrictions on data availability
- For clinical datasets or third party data, please ensure that the statement adheres to our policy

The structural model of MFSD2A-SYNC2 complex have been deposited in Protein Data Bank (PDB) with accession code 7OIX, and corresponding cryo-EM maps were deposited in the Electron Microscopy Data Bank (EMDB) under accession number EMD-12935.

Field-specific reporting

Please select the one below that is the best fit for your research. If you are not sure, read the appropriate sections before making your selection.

☒ Life sciences ☐ Behavioural & social sciences ☐ Ecological, evolutionary & environmental sciences

For a reference copy of the document with all sections, see nature.com/documents/nr-reporting-summary-flat.pdf

Life sciences study design

All studies must disclose on these points even when the disclosure is negative.

Sample size	No statistical methods were used to predetermine sample size. Functional experiments were done in at least n=3 biologically independent experiments. The size of the cryo-EM data set was predetermined based on microscope availability, and data collected was sufficient to obtain maps with the reported resolution that enable structure determination.
Data exclusions	No functional data was excluded from the analyses. Poor-quality cryo-EM micrographs and particles were removed using standard analysis software and protocols
Replication	Functional studies were repeated during biologically experiments as stated in Figure legends and Methods, and results were replicated reasonably well within the experimental error reported. For structural studies, the quality of purified protein and EM specimen was fully reproducible using at least three independent biological replicates
Randomization	Randomization is not relevant to this study
Blinding	Blinding was not performed, because grouping was not applicable to this study

Reporting for specific materials, systems and methods

We require information from authors about some types of materials, experimental systems and methods used in many studies. Here, indicate whether each material, system or method listed is relevant to your study. If you are not sure if a list item applies to your research, read the appropriate section before selecting a response.

Materials & experimental systems

n/a	Involved in the study
☒	☐ Antibodies
☐	☒ Eukaryotic cell lines
☒	☐ Palaeontology and archaeology
☒	☐ Animals and other organisms
☒	☐ Human research participants
☒	☐ Clinical data
☒	☐ Dual use research of concern

Methods

n/a	Involved in the study
☒	☐ ChIP-seq
☒	☐ Flow cytometry
☒	☐ MRI-based neuroimaging

Eukaryotic cell lines

Policy information about cell lines

Cell line source(s)	HEK293F (Thermo Fisher), HEK-293T.17 (ATCC)
Authentication	No cell-line authentication was performed
Mycoplasma contamination	No mycoplasma contamination tests were performed
Commonly misidentified lines (See ICLAC register)	No commonly misidentified cell lines were used